Kinesin-3 and kinesin-1 motors direct basement membrane protein secretion to a basal sub-region of the basolateral plasma membrane in epithelial cells

Allison L. Zajac[1] and Sally Horne-Badovinac[1]*
[1]Department of Molecular Genetics and Cell Biology, The University of Chicago
*corresponding author, shorne@uchicago.edu

Highlights

- A kinesin-3 and a kinesin-1 are required for normal basement membrane (BM) assembly
- Kinesins move Rab10+ BM secretory vesicles basally on polarized microtubule arrays
- Transport biases BM exocytosis to basal subregions of the basolateral membrane
- Loss of kinesins creates ectopic BM networks that disrupt tissue architecture

SUMMARY

Basement membranes (BMs) are sheet-like extracellular matrices that line the basal surfaces of all epithelia. Since BM proteins form networks, they likely need to be secreted near the basal surface. However, the location of their secretion site and how it is selected are unknown. Working in the *Drosophila* follicular epithelium, we identified two kinesins essential for normal BM formation. Our data suggest the two kinesins work together to transport Rab10+ BM protein-filled secretory vesicles towards the basal surface along the polarized microtubule array common to epithelia. This kinesin transport biases BM protein secretion basally. When kinesins are depleted, BM proteins are mis-secreted to more apical regions of the lateral membrane, creating ectopic BM protein networks between cells that disrupt cell movements and tissue architecture. These results introduce a new transport step in the BM protein secretion pathway and highlight the importance of controlling the sub-cellular exocytic site of network-forming proteins.

INTRODUCTION

The basement membrane (BM) is a sheet-like extracellular matrix present in most organs in the body that plays essential roles in tissue development and physiology (Jayadev and Sherwood, 2017; Ramos-Lewis and Page-McCaw, 2018). BMs provide attachment sites for cells, are a reservoir of growth factors, and provide mechanical support to shape tissues. The main structural components of the BM are type IV collagen (Col IV), laminin, heparan sulfate proteoglycans like perlecan, and nidogen/entactin. Many other proteins are found in BMs, and variations in both protein composition and structure allow BMs to carry out important tissue-specific functions like filtering blood in the kidney (Miner, 2012), forming the transparent high refractive index lens capsule in the eye (Danysh and Duncan, 2009), and mechanically protecting muscle fibers (Sanes, 2003). Despite the ubiquity of BMs and their many essential functions, we know little about how BM proteins are secreted, and ultimately assembled, in the correct place within a tissue.

In this study, we investigate how a single sheet of BM is built at the basal surface of an epithelium. BM proteins can be secreted from other tissues and/or produced by the epithelial cells themselves; we focus on epithelial cell-produced BMs. Epithelial cells generate and maintain their polarized membrane domains in part through sorting newly made proteins into apically- or basolaterally-directed secretory pathways (Rodriguez-Boulan and Macara, 2014). Basolateral proteins are generally thought to be secreted through an apical region of the lateral membrane where Par-3 acts as a receptor for the exocyst vesicle tethering complex (Ahmed and Macara, 2017; Kreitzer et al., 2003; Polishchuk et al., 2004). However, BM proteins are large, network-forming proteins, suggesting their secretion site may need to be closer to the basal surface to prevent the assembly of ectopic networks. The secretion site for BM proteins in any epithelium is unknown.

Much of what is known about the polarized secretion of BM proteins comes from studies of the follicular epithelium of *Drosophila*. This somatic epithelium surrounds a cluster of germ cells to form an ovarian follicle (egg chamber) that will produce one egg (Figure 1A) (Horne-Badovinac and Bilder, 2005). The follicular epithelial cells (follicle cells) make their own BM proteins and build a BM on the egg chamber's outer surface (Figure 1A-C). These features allow high-resolution, live imaging of intracellular BM protein trafficking and BM assembly in an intact, developing tissue. Moreover, the powerful genetic approaches in this system have allowed our lab and others to begin to unravel the molecular logic regulating polarized BM protein secretion, including identification of two small GTPases, Rab10 and Rab8, that are required to sort BM proteins into a basally-directed trafficking route (Denef et al., 2008; Devergne et al., 2014, 2017; Isabella and Horne-Badovinac, 2016; Lerner et al., 2013).

47 Studies of the follicle cells have also shown that the location where new BM proteins are secreted can
48 affect the architecture of the resulting BM network. During egg chamber development, the follicular BM
49 becomes mechanically anisotropic. The BM is stiffer around the center of the egg chamber and softer
50 at the ends (Crest et al., 2017), allowing it to act as a “molecular corset” (Gutzeit, 1991) that constrains
51 growth in one direction, promoting tissue elongation as the egg chamber develops (Figure S1A) (Crest
52 et al., 2017; Gutzeit, 1991). One important contributor to the stiffness of this BM is the organization of a
53 subset of BM proteins into an aligned array of fibril-like structures (Chlasta et al., 2017; Crest et al.,
54 2017), which are created by coupling BM protein secretion with the collective migration of follicle cells
55 along the BM (Figures 1B-C and Movie 1) (Isabella and Horne-Badovinac, 2016). During this process,
56 some BM protein secretion is targeted to the lateral membrane, which allows this population of BM
57 proteins to form nascent fibrils in the space between the cells (Figure 1B). Attachment of a nascent fibril
58 to the BM then causes it to be drawn out onto the BM sheet as cells migrate away from this anchor
59 point (Figures 1B and 1C). From our work on BM fibril formation, we proposed that BM protein
60 secretion may be restricted to basal regions of the lateral membrane and basal surface. However,
61 where BM protein exocytosis occurs in the follicle cells and the mechanisms that direct secretion to this
62 site remain to be determined.

63 One potential mechanism to bias the site of BM protein secretion to basal regions of the plasma
64 membrane is suggested by the organization of MTs in epithelial cells. These cells have a polarized
65 array of MTs whose minus ends are anchored apically and plus ends grow toward the basal surface
66 (Figure 1A) (Sanchez and Feldman, 2017). MTs in mammalian epithelial cells are required for polarized
67 BM protein secretion (Almeida and Stow, 1991; Boll et al., 1991). Since MT plus ends are enriched
68 basally, transport of BM protein-filled secretory vesicles by plus end-directed kinesin motors could bias
69 secretion to regions of the plasma membrane near the BM. Vesicular transport often requires multiple
70 different kinesins, whose distinct properties allow them to collectively navigate the crowded cytoplasm
71 and carry their cargo to the correct destination in the cell (Burute and Kapitein, 2019; Hancock, 2014).
72 However, the mechanistic role MTs play in BM protein secretion, and whether kinesins mediate this
73 process, are unknown.

74 Here we show that kinesin-based transport biases the site of BM protein secretion to the basal-most
75 regions of the basolateral plasma membrane. Our data support a model in which the combined activity
76 of the kinesin-3 motor, Khc-73, and the kinesin-1 motor, Khc, are needed to transport Rab10+ BM
77 protein-filled vesicles along the polarized MT array to the correct secretion site near the basal surface.
78 When this transport is reduced, some BM proteins are mis-secreted through more apical regions of the
79 lateral membrane. This leads to the formation of an ectopic BM network between cells that impedes

80 epithelial cell migration and disrupts tissue structure. These results introduce a new transport step in
81 the BM protein secretion pathway and highlight the importance of controlling the sub-cellular exocytic
82 site of network-forming proteins.

83 **RESULTS**

84 **Khc-73 biases BM protein secretion to basal cellular regions**

85 MTs have been implicated in polarized BM protein secretion in mammalian epithelial cells (Almeida and
86 Stow, 1991; Boll et al., 1991), but how they influence this process is unknown. To ask if MTs play a
87 similar role in follicle cells, we depleted them by overexpressing the MT-severing protein spastin
88 (Sherwood et al., 2004), and visualized the BM using an endogenously GFP-tagged α2 chain of type IV
89 collagen (Col IV-GFP) that produces functional Col IV (Buszczak et al., 2007). In control cells, Col IV-
90 GFP is predominantly localized to the BM, with only small Col IV-GFP punctae along lateral surfaces
91 (Figures 1D-F). In cells depleted of MTs, lateral Col IV-GFP is significantly increased (Figures 1D-F and
92 S1B). Therefore, MTs are also involved in BM protein secretion in follicle cells where they bias Col IV
93 accumulation to basal cellular regions.

94 We hypothesized that MTs may serve as polarized tracks for the transport of secretory vesicles filled
95 with BM proteins toward the basal surface. Given the polarity of these MTs (Figure 1A) (Clark and Jan,
96 1997; Khanal et al., 2016; Nashchekin et al., 2016), this model suggests that transport should depend
97 on a plus end-directed kinesin motor. Through an RNAi-based screen, we identified the kinesin-3 family
98 member Khc-73 (human homolog KIF13B) as a candidate. We used CRISPR to generate a new allele,
99 *Khc-73$^{3-3}$*, that has an early stop codon in the motor domain (Figure S1C and Supplemental Table 3).
100 *Khc-73$^{3-3}$* cells have ectopic accumulation of Col IV-GFP along lateral surfaces, similar to what we saw
101 with spastin overexpression (Figures 1D-F). Placing the new *Khc-73$^{3-3}$* allele in trans to the existing
102 *Khc-73^{149}* allele (Liao et al., 2018), also causes lateral Col IV-GFP accumulation (Figures S1D and
103 S1E), confirming that mutation of Khc-73 is the source of this defect. Loss of Khc-73 similarly affects
104 two other BM proteins, laminin and perlecan (Figure 1G). We know that the ectopic Col IV-GFP is in the
105 extracellular space between cells because it is accessible to anti-GFP nanobodies in non-
106 permeabilized tissue (Figure S1F). Therefore, BM proteins are secreted from *Khc-73$^{3-3}$* cells but
107 accumulate in the wrong location.

108 Our investigation of Khc-73 was motivated by the hypothesis that it transports vesicular cargo, like
109 many kinesin-3 family members (Siddiqui and Straube, 2017). However, kinesins can play many roles
110 in epithelial cells (Kreitzer and Myat, 2018). Apical-basal cortical polarity, the polarized localization of
111 transmembrane proteins to apical and lateral membranes, the localization of Col IV-encoding mRNAs,
112 and MT organization are all normal in *Khc-73$^{3-3}$* cells (Figures 1D, S2A-D, and S3A-G). These data
113 suggest that epithelial cell organization remains intact in the absence of Khc-73, lending support to the
114 idea that Khc-73 affects BM protein secretion through vesicular transport.

115 The pattern of ectopic BM protein accumulation in *Khc-73*$^{3-3}$ epithelia is distinct from that caused by loss
116 of previously identified regulators of polarized BM protein secretion in follicle cells, which all cause BM
117 proteins to be mis-sorted into an apically directed secretory pathway (Denef et al., 2008; Devergne et
118 al., 2014, 2017; Isabella and Horne-Badovinac, 2016; Lerner et al., 2013). For example, loss of Rab10
119 leads to abundant apical secretion of Col IV-GFP which forms a web-like network in the space between
120 the apical surface and germ cells, with only minor Col IV-GFP accumulation along lateral surfaces
121 (Figure 1D). In contrast, most of the ectopic Col IV-GFP in *Khc-73*$^{3-3}$ cells is below the zonula adherens
122 (ZA), which demarcates the lateral from the apical domain (Figures 2A and 2B). The lateral Col IV-GFP
123 accumulations appear biased to an apical (upper) region of the lateral domain below the ZA in these
124 egg chambers, which have nearly completed new Col IV production (Figure 2A). However, if we look
125 earlier in development when synthesis of Col IV is high, significantly more extracellular Col IV-GFP
126 accumulates along the entire length of the lateral domain in *Khc-73*$^{3-3}$ cells within a mosaic tissue
127 (Figures 2C-E and S1F). The biased accumulation of Col IV-GFP below the ZA later in development is
128 likely due to the normal movement of nascent fibrils onto the BM, which clears the basal (lower) regions
129 of the lateral domain (Figure 2F). The site of ectopic Col IV-GFP accumulation in *Khc-73*$^{3-3}$ tissue
130 suggests that BM proteins are sorted into a basolateral trafficking pathway, but that their secretion site
131 shifts to include upper regions of the lateral membrane (Figure 2F).

132 Altogether, these data suggest a model in which Khc-73 biases BM protein secretion to basal regions of
133 the basolateral plasma membrane to facilitate their assembly into a single BM sheet at the basal
134 surface.

135 **Khc-73 transports Rab10+ BM protein secretory compartments to basal regions of the cell**
136 To determine how Khc-73 biases the site of BM protein secretion, we focused on the internal
137 membrane compartments that mediate this process. Under normal conditions, we can only detect
138 intracellular Col IV-GFP in the endoplasmic reticulum (ER), preventing us from directly following Col IV-
139 GFP during secretion (Figure S4A). As an alternate marker of BM protein secretory vesicles, we used
140 Rab10. Rabs help to define different membrane compartments by recruiting a variety of effectors
141 (Stenmark, 2009). Rab10 directs secretory transport in other systems (Chen et al., 2012; Deng et al.,
142 2014; Schuck et al., 2007; Zou et al., 2015), and also interacts with the human homolog of Khc-73,
143 KIF13B (Etoh and Fukuda, 2019). In follicle cells, YFP-Rab10 localizes near the Golgi, which in
144 *Drosophila* is distributed among all ER exit sites (ERES), and is where BM protein secretory vesicles
145 likely form (Figures 3A and 3B) (Lerner et al., 2013). In addition, YFP-Rab10 is found on punctate and
146 tubular compartments along the basal surface that preferentially accumulate at the trailing edge of each

147 migrating cell (Lerner et al., 2013), where Khc-73 is also enriched (Figures 3A and 3C). As these
148 compartments are localized away from the Golgi, they likely represent secretory intermediates.

149 To understand the organization of the MTs that may be used to transport Rab10+ compartments
150 toward the basal surface, we examined them in 3D. Similar to other epithelia, one MT array runs
151 parallel to the apical-basal axis of follicle cells (Figure 3D), with minus ends anchored apically and plus
152 ends growing toward the basal surface (Figure 1A) (Clark and Jan, 1997; Khanal et al., 2016;
153 Nashchekin et al., 2016). Follicle cells also have a MT array along their basal surfaces that is thought to
154 be involved in collective migration (Chen et al., 2016; Viktorinová and Dahmann, 2013). These MTs are
155 aligned parallel to the direction of migration (Figure 1E), and their plus ends grow preferentially toward
156 trailing cell edges (Figures 1A) (Viktorinová and Dahmann, 2013). In 3D image volumes taken near the
157 basal surface, we found a connection between these two MT arrays. The basal MT bundles lie flat
158 along part of the basal surface, but bend sharply near the leading edge of cells, integrating seamlessly
159 into the apical-basal array (Figure 3E and Movie 2). This MT organization could allow kinesins to bring
160 Rab10+ secretory vesicles from all over the cell to the basal trailing edge where Rab10+ compartments
161 are enriched (Figure 3F).

162 To determine if Rab10+ punctae move directionally along MTs as expected for a kinesin cargo, we
163 focused on the basal surface because its location on the exterior of the tissue provides superior
164 imaging quality and we can follow the population of Rab10+ punctae that likely mediate basally
165 polarized secretion. YFP-Rab10+ punctae localize to MTs and move rapidly along them (Figure 3G and
166 Movie 3). We frequently observed motile punctae enter the focal plane at leading edges in regions
167 where a MT bundle also came into view (Figure 3G' and Movie 2), suggesting that these bent MTs are
168 used for transport from more apical regions to the basal surface. Finally, we tracked the direction of
169 rapidly moving YFP-Rab10+ punctae and found that they moved toward the trailing edge of cells 2.12-
170 fold more often than toward the leading edge (297 trajectories in 5 egg chambers, data also used as
171 control in Figures 4F-H). This directional bias is consistent with a role for MT plus end-directed
172 transport of Rab10+ secretory vesicles to basal trailing cell edges (Figure 3F).

173 We next asked if Khc-73 is the motor that transports Rab10+ compartments basally. Loss of Khc-73
174 reduces YFP-Rab10 intensity at basal trailing cell edges, but not at the Golgi (Figures 4A and 4B). This
175 result is consistent with our observations of extracellular Col IV-GFP accumulation that suggest Khc-73
176 is not needed for secretion to occur, just to specify the correct location (Figures 2C-E). Conversely,
177 overexpressing Khc-73 increases YFP-Rab10 intensity at basal trailing cell edges, where it forms large,
178 aberrant foci (Figures 4C and 4D). We do not normally see Col IV-GFP colocalized with Rab10 in

control cells. However, Col IV-GFP is concentrated within the aberrant foci induced by Khc-73 overexpression (Figures 4C and 4D), which suggests the foci are clusters of trapped BM protein vesicles. In support of this idea, the foci lack markers of earlier secretory compartments like the ER and Golgi (Figures S4B and S4C), and YFP-Rab10+ tubulovesicular structures move rapidly into and out of the foci (Movie 4). These data show Khc-73 is necessary for Rab10+ compartment localization to the basal surface, and sufficient to alter the localization of Rab10+ and Col IV+ compartments when over-expressed.

Altogether, our observations that Rab10+ punctae move preferentially toward cellular regions enriched in growing MT plus-ends, and that changes in Khc-73 expression affect the localization of both Rab10+ and Col IV+ compartments, strongly suggest that Khc-73 transports BM protein secretory vesicles basally to their secretion site (Figure 4E).

Kinesin-1 works with Khc-73 to direct BM protein secretion basally

Khc-73 is the only motor whose individual knock-down perturbed Col IV secretion in our RNAi screen. However, live imaging and tracking of YFP-Rab10+ punctae movements in *Khc-73*$^{3-3}$ tissue revealed that the YFP-Rab10+ punctae that do reach the basal surface move at normal speeds (control: 0.72 ± 0.21 and *Khc-73*$^{3-3}$: 0.71 ± 0.31 μm/s), although with slightly less directional bias toward the trailing edge of cells (Figures 4F-H, and Movie 5). When multiple kinesins contribute to transport, the cargo speed can be dominated by one motor (Arpağ et al., 2014, 2019; Norris et al., 2014). Since kinesin-1 transports secretory vesicles to specify the secretion site of many proteins (Fourriere et al., 2019), and more specifically transports Rab10+ vesicles in mammalian neurons (Deng et al., 2014), we investigated if *Drosophila's* sole kinesin-1 motor, Khc, might work with Khc-73 to transport Rab10+ BM protein secretory vesicles.

To test this hypothesis, we depleted both kinesins. Compared to depletion of Khc-73 alone, co-depletion of Khc-73 and Khc using RNAi caused Col IV-GFP to accumulate at lateral cell edges at higher levels (Figures 5A-C). We confirmed that loss of Khc alone does not cause lateral Col IV-GFP accumulation using a Khc null mutation, *Khc*^{27} (Figures S5A and S5B) (Brendza et al., 1999). Co-depletion of Khc-73 and kinesin light chain (Klc), which often acts as a cargo adaptor for Khc (Kamal and Goldstein, 2002), similarly enhanced lateral Col IV-GFP accumulation (Figures 5A-C). These dual RNAi experiments uncovered that Khc and Klc work with Khc-73 to promote basally polarized BM protein secretion.

209 We next asked if Khc affects BM protein secretion by the same mechanism as Khc-73, transporting
210 Rab10+ compartments toward the basal surface. Since Khc loss alone is insufficient to disrupt the site
211 of polarized Col IV-GFP secretion (Figures S5A and S5B), we expected a milder reduction in YFP-
212 Rab10+ compartments at the basal trailing edges of *Khc*^{27} cells than in *Khc-73*$^{3-3}$ cells (Figures 4A and
213 4B). Surprisingly, this population of YFP-Rab10+ compartments is instead increased in *Khc*^{27} cells
214 (Figures 6A and 6B). Khc has two roles that could impact the localization of Rab10+ compartments;
215 Khc transports vesicles and also rearranges the MT tracks themselves by binding a second MT with its
216 tail domain and sliding the two MTs relative to each other (Jolly et al., 2010). MTs remain aligned in
217 *Khc*^{27} cells (Figures S5C-E), and a mutation in Khc's tail domain that selectively impairs its ability to
218 slide MTs does not affect YFP-Rab10+ compartment localization (Figures 6A and 6B) (Winding et al.,
219 2016). These data point to Khc's cargo transport activity contributing to the normal localization pattern
220 of Rab10+ compartments.

221 The increase in Rab10+ compartments at the basal surface in *Khc*^{27} mutant cells was unexpected. We
222 hypothesized that loss of Khc is compensated for by increased Khc-73 activity, and that high Khc-73
223 activity changes Rab10+ compartment localization. In support of this idea, the increase in YFP-Rab10+
224 compartments at the basal trailing edges of *Khc*^{27} cells resembles the aberrant YFP-Rab10+ foci that
225 form when Khc-73 is overexpressed (Figures 4C and 4D). In addition, Khc-73-GFP levels are increased
226 at the basal trailing edges of *Khc*^{27} cells (Figures 6C and 6D). Finally, removal of both kinesins
227 prevented nearly all YFP-Rab10+ compartment accumulation at basal trailing edges (Figures 6F and
228 6G), showing that Khc-73 mediates the increase. These data suggest that while Khc normally
229 contributes to the transport of Rab10+ BM protein secretory vesicles (Figure 6E), Khc-73 can largely
230 compensate for its loss. However, increased reliance on Khc-73 leads to more Rab10+ compartment
231 localization to basal trailing cell edges (Figures 6A and 6B), revealing a distinct role for Khc in achieving
232 the normal distribution of Rab10+ compartments.

233 Further reducing kinesin levels by expressing *Khc*^{RNAi} in *Khc-73*$^{3-3}$ cells, as we did to visualize Rab10
234 above, produced a new phenotype; Col IV-GFP accumulated on the apical surface (Figure 6H). In
235 these cells, YFP-Rab10+ compartments are not only lost from the basal surface but also become
236 concentrated beneath the apical surface (Figures 6I-K). Importantly, general cell organization is
237 unaffected in *Khc*^{RNAi} & *Khc-73*$^{3-3}$ cells, as the polarized localization of cortical and transmembrane
238 proteins, Col IV-encoding mRNAs and MTs all remain normal (Figures 6H and S6A-G). Therefore,
239 these two kinesins not only contribute to post-Golgi BM protein secretory vesicle transport, but also play
240 an essential role in preventing apical secretion of BM proteins that is only revealed when they are
241 severely depleted.

242 **Intercellular BM protein networks disrupt epithelial architecture**

243 Finally, we investigated how changing the subcellular secretion site of BM proteins impacts the final
244 structure of the BM and the follicle cells migrating along it. We initially focused on the BM sheet along
245 the basal surface. The mean level of Col IV-GFP in the BM is normal in all genotypes where kinesins
246 are reduced, except the condition that causes apical BM protein secretion, *Khc-73*$^{3-3}$ & *Khc*^{RNAi} (Figures
247 7A and B). However, there are striking changes to the structure of the BMs in all conditions. There are
248 more and larger fibrils in *Khc-73*$^{3-3}$ BMs and *Khc-73*^{RNAi} & *Khc*^{RNAi} BMs (Figures 7A and 7D). Therefore,
249 in these kinesin mutant conditions, although Col IV is initially mis-secreted all along the lateral
250 membrane, much of this protein is eventually moved onto the underlying BM as fibrils (Figure 2F).

251 We know that these kinesin mutant conditions also have persistent lateral accumulations of Col IV. To
252 understand how this Col IV is organized relative to follicle cells, we made 3D reconstructions of the Col
253 IV-GFP that is not in the BM. In reconstructions of the apical secretion condition, *Khc-73*$^{3-3}$ & *Khc*^{RNAi}, a
254 web-like Col IV-GFP network lies atop the apical surface of follicle cells (Figure 7C). In contrast, in
255 conditions that cause lateral secretion, Col IV-GFP forms an intercellular network that spans multiple
256 cell lengths (Figure 7C). Some regions of these lateral, intercellular networks are connected to the
257 underlying BM. As follicle cells are collectively migrating relative to the BM, these connections likely act
258 as anchor points that impede cell movement. This is best illustrated in the mildest condition, *Khc-73*$^{3-3}$,
259 where there are only a few, isolated Col IV-GFP cables running between cells and anchored to the BM
260 at one end (Figure 7E, arrows, and Movie 6). The hexagonal packing of follicle cells is disrupted
261 specifically near these cables compared to other areas of the epithelium (Figure 7E). Even more
262 strikingly, several nuclei are highly deformed (Figure 7E). Since follicle cells collectively migrate in a
263 tightly packed sheet, some cells are likely forced to squeeze through the intercellular Col IV-GFP
264 network, causing this nuclear deformation. This drastic effect on cells from only a relatively small
265 fraction of Col IV within these cables highlights the importance of tightly controlling the secretion site of
266 these network-forming proteins.

267 **DISCUSSION**

268 This work provides the first mechanistic insight into how the secretion site of BM proteins is controlled
269 in an epithelium. Like mammalian epithelia, we found that MTs influence polarized BM protein secretion
270 in follicle cells. We further identified a kinesin-3 motor, Khc-73, and a kinesin-1 motor, Khc, required for
271 this process. When these motors are depleted, BM proteins form ectopic networks between follicle
272 cells. Reducing kinesin levels also alters the localization and movement of Rab10+ BM protein-filled
273 secretory compartments. The impact of kinesin depletion on the localization of both intracellular
274 Rab10+ compartments, and extracellular ectopic Col IV accumulations, lead us to propose that these
275 two kinesins transport BM protein-filled secretory vesicles towards the basal surface to bias the site of
276 BM protein secretion to basal cellular regions.

277 How are kinesins recruited to BM protein secretory vesicles? We previously showed that Rab10 is
278 required to sort BM proteins into a basally directed trafficking pathway and that it localizes near the
279 Golgi where secretory vesicles likely form (Lerner et al., 2013). Based on Rab10's role in trafficking
280 other types of secretory vesicles (Chen et al., 2012; Deng et al., 2014; Schuck et al., 2007; Zou et al.,
281 2015), it is likely that Rab10 remains associated with BM protein secretory vesicles during transport to
282 the cell surface, recruiting different effectors over time to execute subsequent trafficking steps. We
283 envision that Rab10 recruits the kinesins to newly formed BM protein-filled vesicles near the Golgi to
284 initiate their basally-directed transport. In mammalian cells, Rab10 interacts with both kinesins we
285 identified. Rab10 directly binds to Khc-73's homolog, KIF13B (Etoh and Fukuda, 2019), and indirectly
286 associates with kinesin-1 via the adaptor protein Jip1 and kinesin light chain (Deng et al., 2014). Rab8
287 is also required for polarized BM protein secretion in follicle cells (Devergne et al., 2017), which raises
288 the possibility that Rab8 recruits the kinesins either alone or in combination with Rab10. To date,
289 however, Rab8 has not been linked to either kinesin in this study. Since kinesins need to not only be
290 recruited, but activated by association with their cargo or other proteins such as adaptors (Fu and
291 Holzbaur, 2014), distinguishing between conservation of these mammalian interactions and other
292 models for how the kinesins are recruited to BM protein vesicles will be an important area for future
293 research.

294 The involvement of both kinesin-3 and kinesin-1 family motors in the transport of Rab10+
295 compartments raises questions about their respective contributions. Individual loss of either Khc or
296 Khc-73 has the opposite effect on Rab10+ compartment localization to basal trailing cell edges,
297 suggesting the two motors make distinct contributions to transport of Rab10+ compartments. Studies of
298 how other kinesin-3 and kinesin-1 family motors contribute to transport when on the same cargo
299 provide a useful framework to think about how they may work together in follicle cells. Kinesins are

300 placed under load during transport by pulling against their cargo, and each other. The ability of kinesin-
301 1 motors to remain bound to MTs better under load than kinesin-3 motors allows kinesin-1 to play a
302 dominant role in the movement of cargo (Arpağ et al., 2014, 2019; Norris et al., 2014). Kinesin-3 family
303 motors detach from MTs easily under load, but they also rebind very quickly, leading to the model that
304 kinesin-3 motors allow cargo to remain attached to MTs in the face of obstacles in the cell (Arpağ et al.,
305 2019; Budaitis et al., 2021; Norris et al., 2014). This, along with kinesin-3's higher speeds and longer
306 run-lengths, allows kinesin-3 motors to facilitate long distance transport (Huckaba et al., 2011; Siddiqui
307 and Straube, 2017; Soppina et al., 2014). These differences in kinesin-1 and kinesin-3 behavior are
308 one important determinant of their contributions to collectively transporting cargo.

309 In follicle cells, loss of Khc-73 alone disrupts polarized BM protein secretion, while loss of Khc alone
310 does not, suggesting the kinesin-3, Khc-73, plays the major role in secretory transport. However, when
311 Khc-73 is removed, although there are fewer Rab10+ punctae at the basal surface, they move at
312 normal speeds. If Khc-73 and Khc are both on the same Rab10+ vesicle, Khc's superior ability to
313 remain attached to MTs under load may allow it to play a dominant role in cargo movement even under
314 normal conditions, and it simply continues to transport Rab10+ vesicles when Khc-73 is missing. Why
315 then are Rab10+ compartments reduced at the basal surface when Khc-73 is missing? Since kinesin-3
316 family motors facilitate long distance transport, Khc-73 loss may reduce the ability of Rab10+
317 compartments to initially associate with, or remain attached to, MTs. Conversely, when Khc-73
318 operates without Khc, it not only compensates for Khc's loss but transports more Rab10+
319 compartments to basal trailing cell edges than normal. Since this location is where growing MT plus
320 ends terminate (Viktorinová and Dahmann, 2013), this is potentially also explained by Khc-73 mediating
321 longer-distance movements of Rab10+ compartments than Khc. Since we only image the basal surface
322 of each cell, we rarely observed the beginning and end of a Rab10+ puncta trajectory, precluding
323 analysis of run lengths. Following the dynamics of Rab10+ compartments in 3D would allow more
324 comprehensive analysis of their movements, and shed new light on how the two kinesins mediate
325 Rab10+ transport from all over the cell to the basal trailing cell edge.

326 A recent study on the human homologs of Khc-73 and Khc, KIF13B and KIF5B, thoroughly dissected
327 their distinct contributions to the transport of Rab6+ secretory vesicles in non-polarized HeLa cells
328 (Serra-Marques et al., 2020). The authors found that both kinesins are needed to bring secretory
329 vesicles all the way to the plus ends of dynamic MTs, spatially determining where secretion occurs
330 (Serra-Marques et al., 2020). This is similar to how we think kinesins specify the site of BM protein
331 secretion. However, in HeLa cells the more highly expressed kinesin-1 motor plays the major role in
332 determining where Rab6+ vesicles fuse with the plasma membrane (Serra-Marques et al., 2020). This

difference highlights the importance of studying the transport of a variety of native cargos *in vivo,* where differences in motor expression, cell polarity, and other key regulators of kinesins like MT-associated proteins and MT modification can influence transport (Guardia et al., 2016; Guedes-Dias et al., 2019; Monroy et al., 2020; Norris et al., 2014; Reed et al., 2006).

Our work also introduces an unusual architecture for an epithelial MT array. Previous studies described two polarized MT arrays in the follicle cells – one running from the apical surface to the basal surface, which is standard in epithelia (Clark and Jan, 1997; Khanal et al., 2016; Nashchekin et al., 2016), and another along the basal surface of the cells, which has been linked to regulation of collective migration (Chen et al., 2016; Viktorinová and Dahmann, 2013). We find these two MT arrays are interconnected, which suggests that MT motors may move cargo seamlessly between the apical-basal and planar MT arrays. Because MT plus ends grow both toward the basal surface and toward the trailing edges of cells, this connection could explain why Rab10+ compartments are enriched at basal trailing edges. Whether this MT arrangement leads to planar-polarized secretion of BM proteins has not yet been directly demonstrated, but we envision that such a mechanism would bring BM protein secretory vesicles all the way to the trailing edge of cells where they may naturally fuse with the lower lateral membrane for secretion to promote BM fibril formation. Although MT motors are known to be important for the secretion of many apical proteins in epithelial cells, little is known about the role of MTs and MT motors in the secretion of basolateral proteins (Rodriguez-Boulan and Macara, 2014). Determining how this MT array is built, and the significance that it holds for polarized membrane traffic, is likely to reveal the strategies cells employ to specify discrete secretion sites within larger plasma membrane domains. In the migrating follicle cells, this will also further our understanding of how cells coordinate migration with secretion.

Our finding that a moderate depletion of kinesins causes BM proteins to accumulate between the lateral membranes of follicle cells is significant because this phenotype is distinct from those caused by mutation of the other known regulators of polarized BM protein secretion in the follicle cells, all of which cause BM proteins to accumulate on the apical surface (Denef et al., 2008; Devergne et al., 2014, 2017; Isabella and Horne-Badovinac, 2016; Lerner et al., 2013). Strong depletion using *Khc-73*$^{3-3}$ & *Khc*^{RNAi}, however, causes BM proteins to accumulate mainly on the apical surface. This result could indicate that, like Rab10, kinesins also play an earlier role in sorting BM proteins into a basolateral pathway. However, a second possibility is suggested by the observation that Rab10+ compartments also relocalize apically when kinesins are strongly depleted. BM proteins may still enter a Rab10+ compartment, but without plus end-directed kinesins present, a minus end-directed motor like dynein could redirect the vesicles apically. If true, this would imply that simply delivering BM protein vesicles to

366 the apical membrane is sufficient for apical secretion in follicle cells, and that titrating the relative levels
367 of plus and minus end-directed motors plays a key role in polarized secretion. New tools to visualize
368 how BM proteins move through the secretory pathway will be needed to distinguish between these
369 models.

370 It is likely that kinesin-based transport integrates with other cellular mechanisms in the follicle cells to
371 ensure BM proteins assemble into a single sheet. Contributions from receptors for BM proteins like
372 integrins and dystroglycan may play a role in determining where BM proteins assemble, and could aid
373 in post-secretion movements of BM proteins such as those required for BM fibril formation (Campos et
374 al., 2020; Jayadev and Sherwood, 2017). We previously showed that Col IV-encoding mRNAs are
375 enriched basally in follicle cells and proposed that local Col IV protein synthesis and export through
376 basally localized Golgis promotes polarized BM protein secretion (Lerner et al., 2013). We re-examined
377 Col IV-encoding mRNAs in this study using a more sensitive detection method and detected more
378 individual Col IV mRNAs distributed throughout the cell. Thus, kinesin-based transport of Rab10+
379 secretory vesicles may ensure that the subset of BM proteins that are synthesized away from the basal
380 surface still reach the correct secretion site. Kinesin-based transport of BM proteins may be particularly
381 important in mammalian cells, where a single, apically localized Golgi apparatus creates an even bigger
382 spatial problem for BM protein secretion.

383 Finally, this work demonstrates that tightly controlling the sub-cellular site of BM protein secretion is
384 critical for epithelial architecture. We previously showed that targeting BM protein secretion to lateral
385 surfaces alters the architecture of the follicular BM in a way that is beneficial for the tissue - it allows the
386 formation of the BM fibrils necessary for normal egg chamber elongation (Isabella and Horne-
387 Badovinac, 2016). It is now clear, however, that BM protein secretion cannot occur anywhere along the
388 lateral membrane, as secretion to the upper region of this domain causes BM protein networks to form
389 between the cells. Moreover, when these ectopic networks attach to the main BM, they act as anchors
390 that locally impede the collective migration of the follicle cells, distorting the cells' shapes to such an
391 extent that even the nuclei are deformed. We imagine that the formation of ectopic BM protein networks
392 between cells would be detrimental to any epithelium undergoing cellular rearrangements. These would
393 include processes like cell division and cell extrusion that are required for tissue growth and
394 homeostasis, as well as processes like cell intercalation and apical constriction that underlie changes in
395 tissue shape (Kozyrina et al., 2020). Given that BM assembly and epithelial morphogenesis often
396 coincide during development (Jayadev and Sherwood, 2017; Walma and Yamada, 2020), we propose
397 that kinesin-based transport of BM proteins toward the basal surface may provide a general mechanism
398 to ensure that these two key aspects of epithelial development do not interfere with one another.

399 **Author Contributions**

400 A.L.Z. and S.H-B. conceived the study. A.L.Z. designed experiments, generated new reagents,
401 performed experiments, analyzed the data, and prepared the figures. A.L.Z. and S.H-B. wrote the
402 manuscript.

403

404 **Acknowledgements**

405 We thank Lynn Cooley, Robin Hiesinger, Nina Sherwood, Pejmun Haghighi, Dan Bergstralh, Vladimir
406 Gelfand, and Chris Doe for *Drosophila* stocks. Younan Li for help with Sobel operator analysis and
407 MATLAB code. Members of the S.H-B., Munro, Fehon, and Glick labs for experimental advice, and
408 members of the S.H-B. lab, Kriza Sy, and Serapion Pyrpassopoulos for comments on the manuscript.
409 Funding was provided by the following: American Heart Association 16POST2726018, American
410 Cancer Society 132123-PF-18-025-01-CSM, and Chicago Biomedical Consortium FP064171-01-PR
411 postdoctoral fellowships to A.L.Z. American Cancer Society RSG-14-176 and NIH R01 GM136961 to
412 S.H-B.

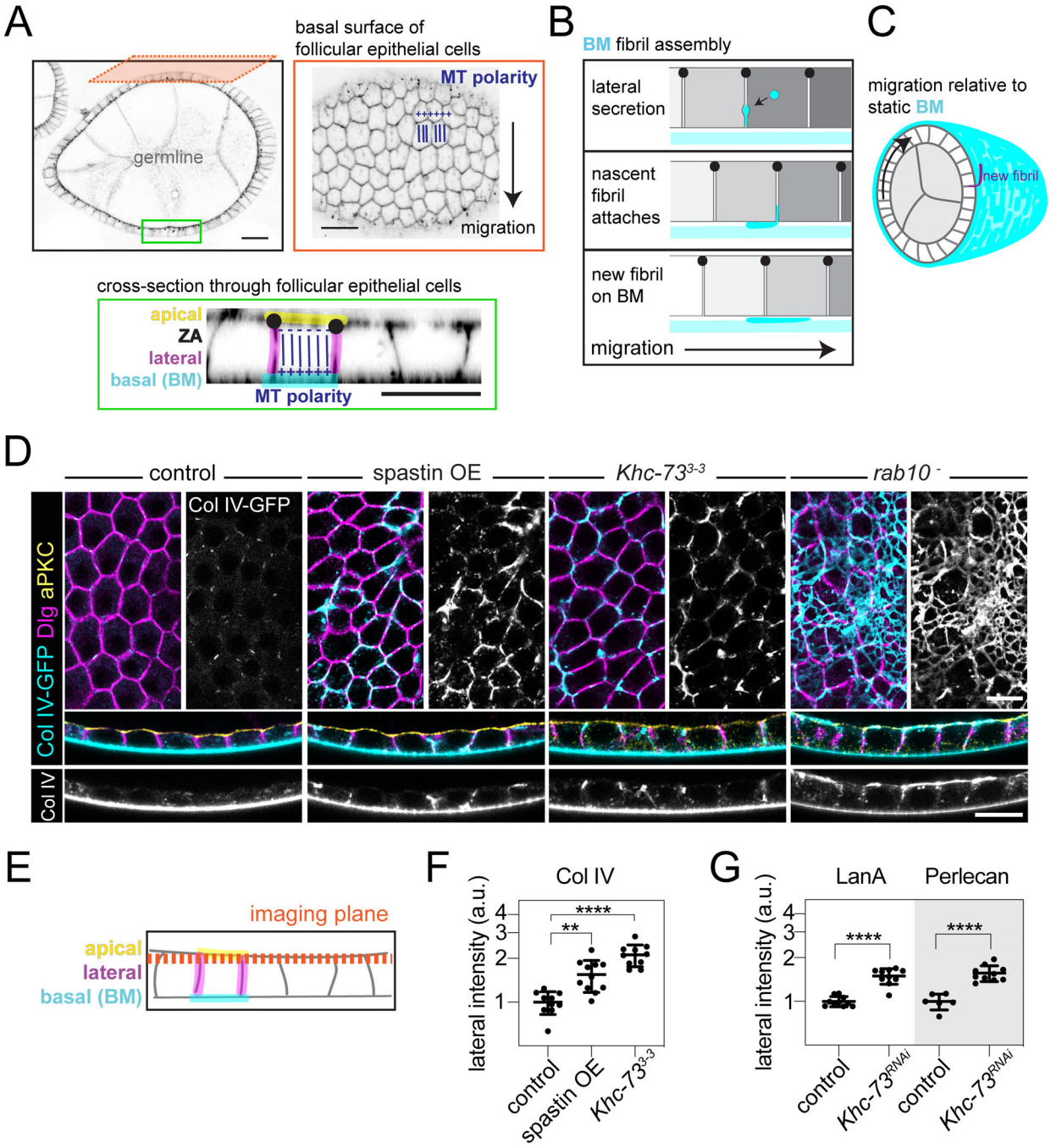

Figure 1. Khc-73 and MTs are required for polarized BM protein secretion

413

414 **Figure 1. Khc-73 and MTs are required for polarized BM protein secretion**

415 A. Images of an egg chamber with cell edges marked with CellMask. The green box highlights
416 follicle cell polarity and MT polarity (ZA, zonula adherens). The orange box highlights a plane
417 along the basal surface with the polarity of the basal MT array indicated relative to the direction
418 of cell migration.

419 B. Illustration of how BM fibrils are formed by lateral secretion, and then drawn out onto the BM
420 during migration.

421 C. Illustration of a transverse section through an egg chamber showing follicle cells collectively
422 migrating along the BM, causing all cells to rotate relative to the static BM while laying down BM
423 fibrils (purple highlight).

424 D. Images of ectopic Col IV-GFP in epithelia overexpressing spastin or mutant for *Khc-73*$^{3-3}$ or
425 *rab10*$^{-}$. Top panels are planes through the lateral domains that capture some of the apical
426 surface due to tissue curvature, as diagrammed in (E). Bottom panels are cross sections. Anti-
427 Dlg marks lateral domains. Anti-aPKC marks apical domains (only shown in cross sections).

428 E. Illustration of imaging planes in (D).

429 F. Quantification of increased Col IV-GFP at lateral cell edges from (D) in epithelia overexpressing
430 spastin or mutant for *Khc-73*$^{3-3}$. Ordinary one-way ANOVA with Dunnett's multiple comparisons
431 test, **p<0.01, ****p < 0.0001. In the order on graph, n= 10,11,10 egg chambers.

432 G. Quantification of increased LanA and Perlecan accumulation at lateral cell edges in control and
433 *Khc-73*^{RNAi} epithelia. Unpaired t test, ****p<0.0001. In the order on graph, n= 10,10,6,10 egg
434 chambers.

435 Stage 8 egg chambers. Data represent mean ± SD plotted on a log scale. Scale bars, (A) 20 μm, all
436 others 10 μm. See also Figure S1 and Movie 1.

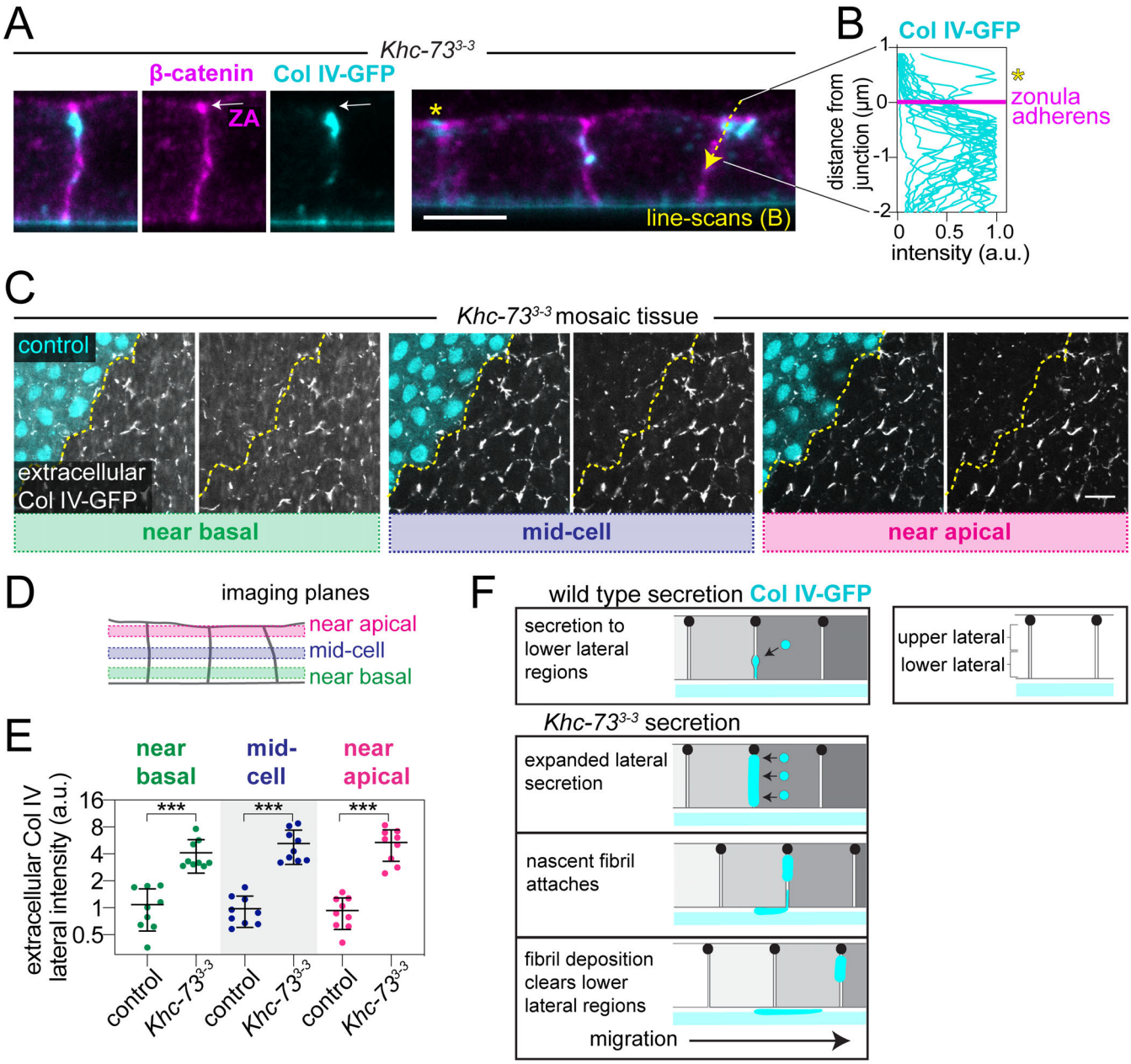

Figure 2. Col IV accumulates all along the lateral domain in *Khc-73*$^{3-3}$ cells

437

Figure 2. Col IV accumulates all along the lateral domain in *Khc-73$^{3-3}$* cells

A. Images of lateral Col IV-GFP in *Khc-73$^{3-3}$* epithelia relative to staining for the zonula adherens (ZA, white arrow). Arrow indicates where intensity line-scans were performed in (B); asterisk highlights example where Col IV-GFP is apical to the ZA.
B. Graph of Col IV-GFP fluorescence intensity along 20 cell-cell interfaces as indicated in (A). Col IV-GFP line-scans were aligned to peak β-cat signal at the ZA, indicated in magenta. Asterisk highlights the example of Col IV-GFP apical to the ZA from (A).
C. Images of ectopic extracellular Col IV-GFP in *Khc-73$^{3-3}$* mosaic tissue at three different z-planes through the lateral domain, diagrammed in (D). The dotted line demarcates control and *Khc-73$^{3-3}$* cells. Extracellular Col IV-GFP is highlighted by staining non-permeabilized tissue with a nanobody to GFP (Figure S1F).
D. Illustration of imaging planes in (C).
E. Quantification of extracellular Col IV-GFP in (C), showing increased lateral accumulation in *Khc-73$^{3-3}$* cells at all three z-planes. Data represent mean ± SD plotted on a log scale. Paired t tests, ***$p<0.001$. n= 9 egg chambers.
F. Model for how loss of Khc-73 leads to lateral Col IV accumulation, which persists mainly in the upper region of the lateral domain.

Stage 8 egg chambers (A, B). Stage 7 egg chambers (C, E). Scale bars, 5 μm (A), 10 μm (B). See also Figures S1, S2, S3.

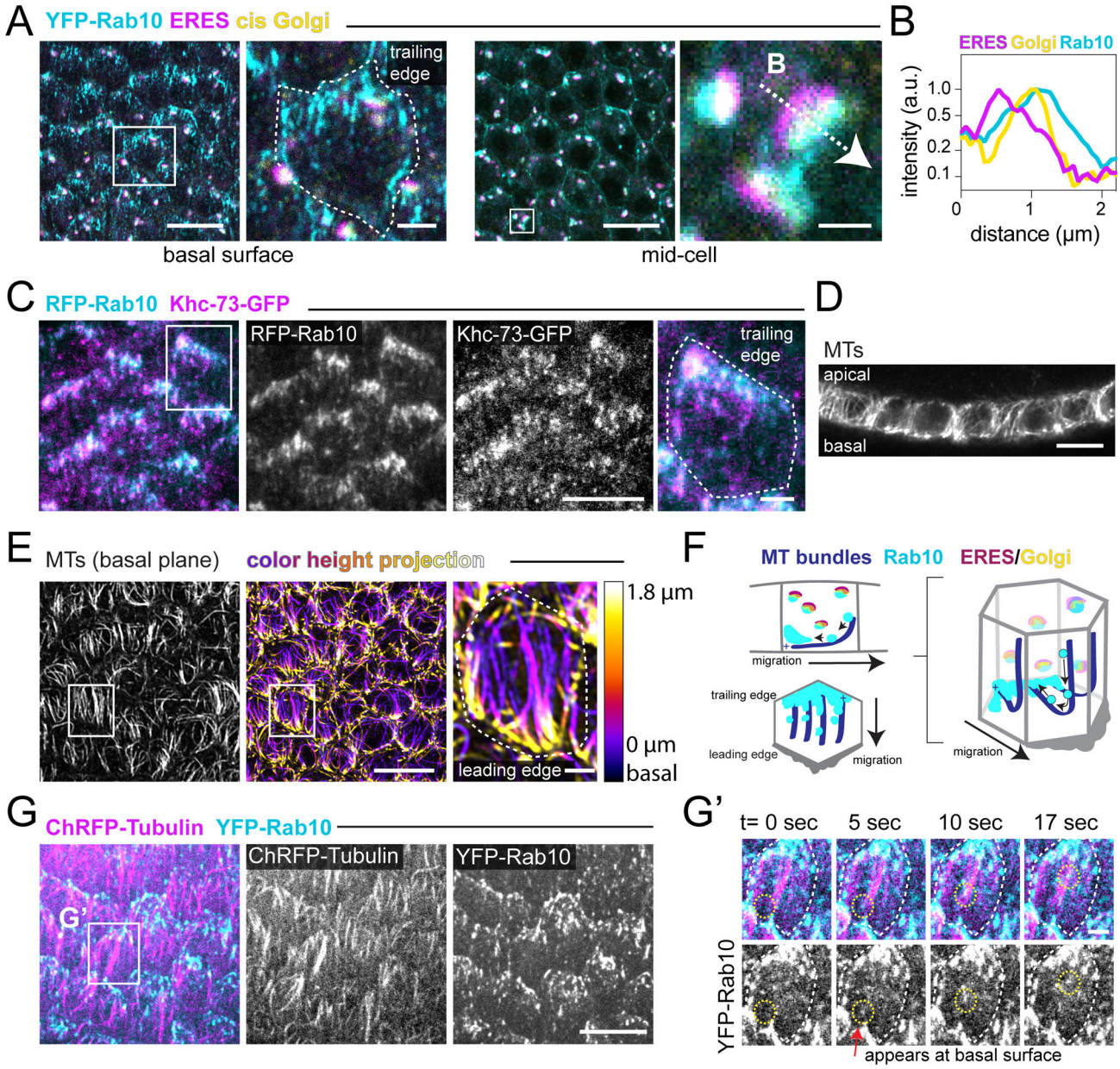

Figure 3. Rab10+ compartments move along MTs to basal trailing cell edges

457

Figure 3. Rab10+ compartments move along MTs to basal trailing cell edges

A. Images of UAS-YFP-Rab10 localization at the basal surface and mid-cell. The mid-cell inset highlights the position of YFP-Rab10 relative to staining for the ERES protein Tango1 and the cis Golgi protein GM130 (line-scan of example intensity profiles in B). The basal inset highlights one cell traced with a dotted line with UAS-YFP-Rab10 at trailing edge. Scale bars, 10 μm main panels, 2 μm basal inset, and 1 μm ERES/Golgi inset.
B. Line-scan of fluorescence intensity along the arrow in (A).
C. Image of Khc-73-GFP (endogenous promoter) localizing to UAS-RFP-Rab10+ tubular compartments at the basal trailing edges of cells. Inset cell traced with dotted line.
D. Image showing MTs (anti-acetylated α-tubulin) aligned along the apical-basal axis in a cross-section through follicle cells.
E. Image of MTs (anti-acetylated α-tubulin) aligned parallel to the direction of migration along the basal surface (left panel). A color height projection (center panel) of the basal-most 1.8 μm of the epithelium shows that the basal MT bundles at the leading edges of cells bend and extend apically. Inset highlights a single cell traced with a dotted line. See also Movie 2.
F. Illustration of the 3D organization of Rab10+ compartments and MT bundles that bend near the basal leading cell edges, as viewed in: cross-section, along the basal surface, or in a 3D cell. Only a few examples of this bent population of MTs/MT bundles are shown for clarity. We could not follow all MTs in 3D in all areas of cell.
G. Image from time-lapse showing that UAS-YFP-Rab10+ compartments colocalize with and move along the basal MT array (UAS-ChRFP-α-tubulin). (G') Montage of YFP-Rab10+ puncta appearing in the focal plane and moving along a MT bundle from inset in G. See also Movie 3.

Stage 7 egg chambers (A, B, C, D, E). Stage 8 egg chamber (G). Images oriented such that migration is down. Scale bars, 10 μm for main panels and 2 μm for cell insets, except as described in (A). See also Figure S4A, Movie 2, and Movie 3.

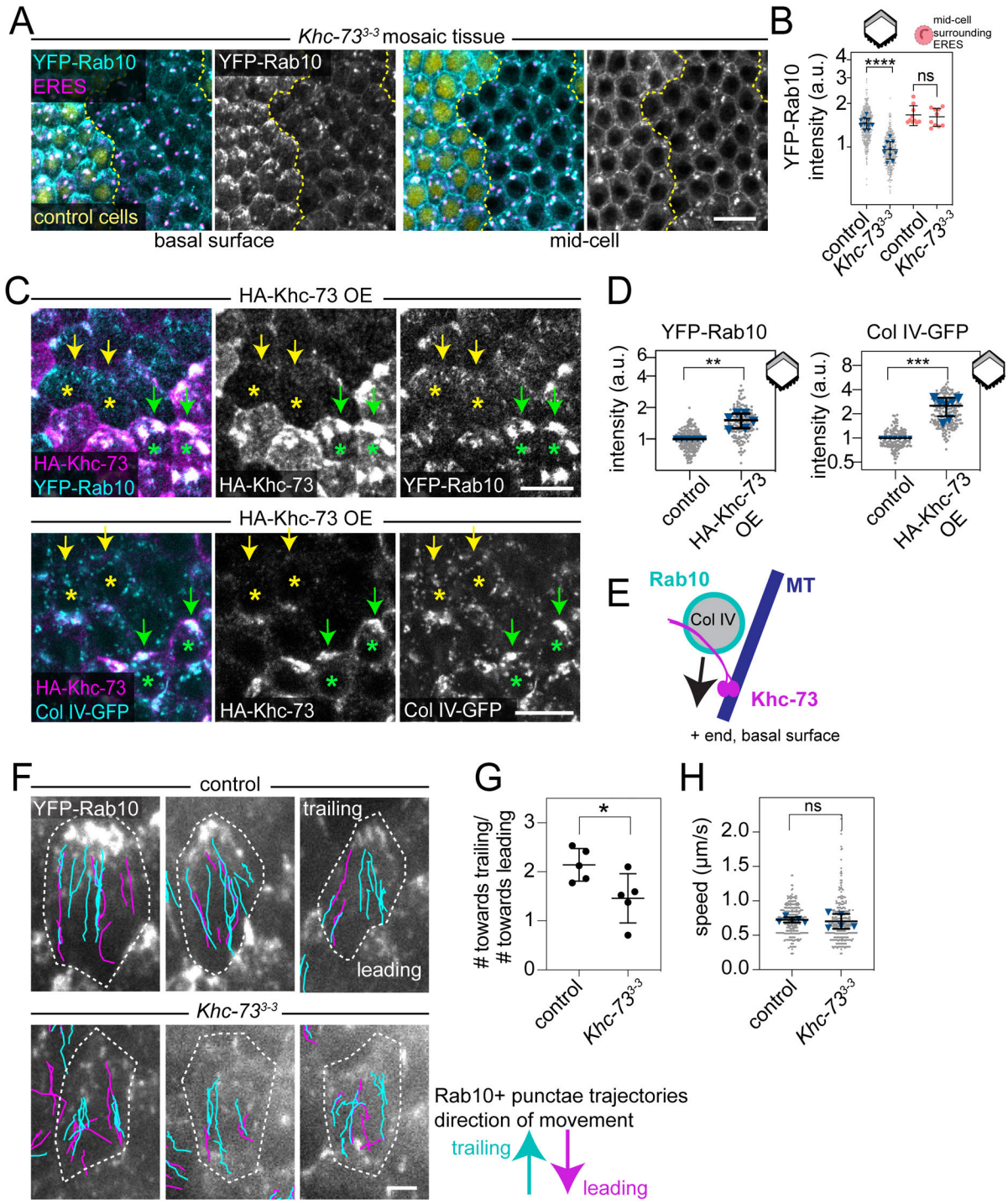

Figure 4. Khc-73 transports Rab10+ compartments to the basal trailing edges of follicle cells

483

Figure 4. Khc-73 transports Rab10+ compartments to the basal trailing edges of follicle cells

A. Images of UAS-YFP-Rab10 and ERES (anti-Tango1) in *Khc-73*$^{3-3}$ mosaic tissue at the basal surface and mid-cell. The dotted line demarcates control and *Khc-73*$^{3-3}$ cells.

B. Quantification of the decrease in UAS-YFP-Rab10 levels at basal trailing cell edges (grey region of cell in cartoon) without a change in UAS-YFP-Rab10 levels near the ERES mid-cell (salmon) in *Khc-73*$^{3-3}$ cells. Grey dots represent individual cells and blue triangles represent egg chamber means. For basal surface: paired t test, ****$p<0.0001$. n=10 egg chambers, 544 control and 457 *Khc-73*$^{3-3}$ cells. For ERES: Wilcoxon matched-pairs signed rank test, ns $p>0.05$. n=10 egg chambers.

C. Images of YFP-Rab10 (endogenous, top panels), and Col IV-GFP (endogenous, bottom panels) in epithelia overexpressing UAS-HA-Khc-73 in patches of cells. YFP-Rab10 images are along basal surface, and Col IV-GFP panels are 1.5 µm above the basal surface to avoid the Col IV-GFP signal within the BM. Yellow asterisks indicate “control” cells negative for HA-Khc-73 staining; yellow arrows point at the trailing cell edges. Green asterisks label HA-Khc-73 OE cells; green arrows point at the punctae accumulating at trailing cell edges. See also Movie 4.

D. Quantification of the increase in YFP-Rab10 (endogenous) and Col IV-GFP (endogenous) in HA-Khc-73 OE cells at basal trailing cell edges (grey region of cell in cartoon). Grey dots represent individual cells and blue triangles represent egg chamber means. One sample t tests compared to the theoretical ratio of 1, **$p<0.01$, ***$p<0.001$. For YFP-Rab10, n=6 egg chambers, 199 “control” and 161 HA-Khc-73 OE cells. For Col IV-GFP, n=7 egg chambers, 149 “control” and 214 HA-Khc-73 OE cells.

E. Model of Khc-73’s role in transporting Rab10+ Col IV-filled secretory vesicles toward the basal surface.

F. Images of example cells (dashed outlines) from the first frame of a time-lapse of control and *Khc-73*$^{3-3}$ epithelia expressing UAS-YFP-Rab10. Trajectories of UAS-YFP-Rab10+ punctae are overlaid on the images and color-coded for direction. See also Movie 5.

G. Quantification of the direction of UAS-YFP-Rab10+ punctae movements from (F) scored as either toward the trailing edge or the leading edge in control and *Khc-73*$^{3-3}$ epithelia. Unpaired t test, *$p<0.05$. n= 5 egg chambers, 297 runs in control and 305 runs in *Khc-73*$^{3-3}$ egg chambers.

H. Distribution of speeds of UAS-YFP-Rab10+ punctae in control and *Khc73*$^{3-3}$ epithelia at the basal surface. Grey dots represent individual runs and blue triangles represent egg chamber means. Unpaired t test, ns $p>0.05$. n= 5 egg chambers, 297 runs in control and 305 runs in *Khc-73*$^{3-3}$ egg chambers.

Stage 7 egg chambers. Images oriented such that migration is down. Data represent mean ± SD. Statistics were performed on egg chamber mean values. Data in B and D are plotted on a log scale. Scale bars, 10 µm (A and C), 2 µm (F). See also Figure S4B, S4C, Movie 4, and Movie 5.

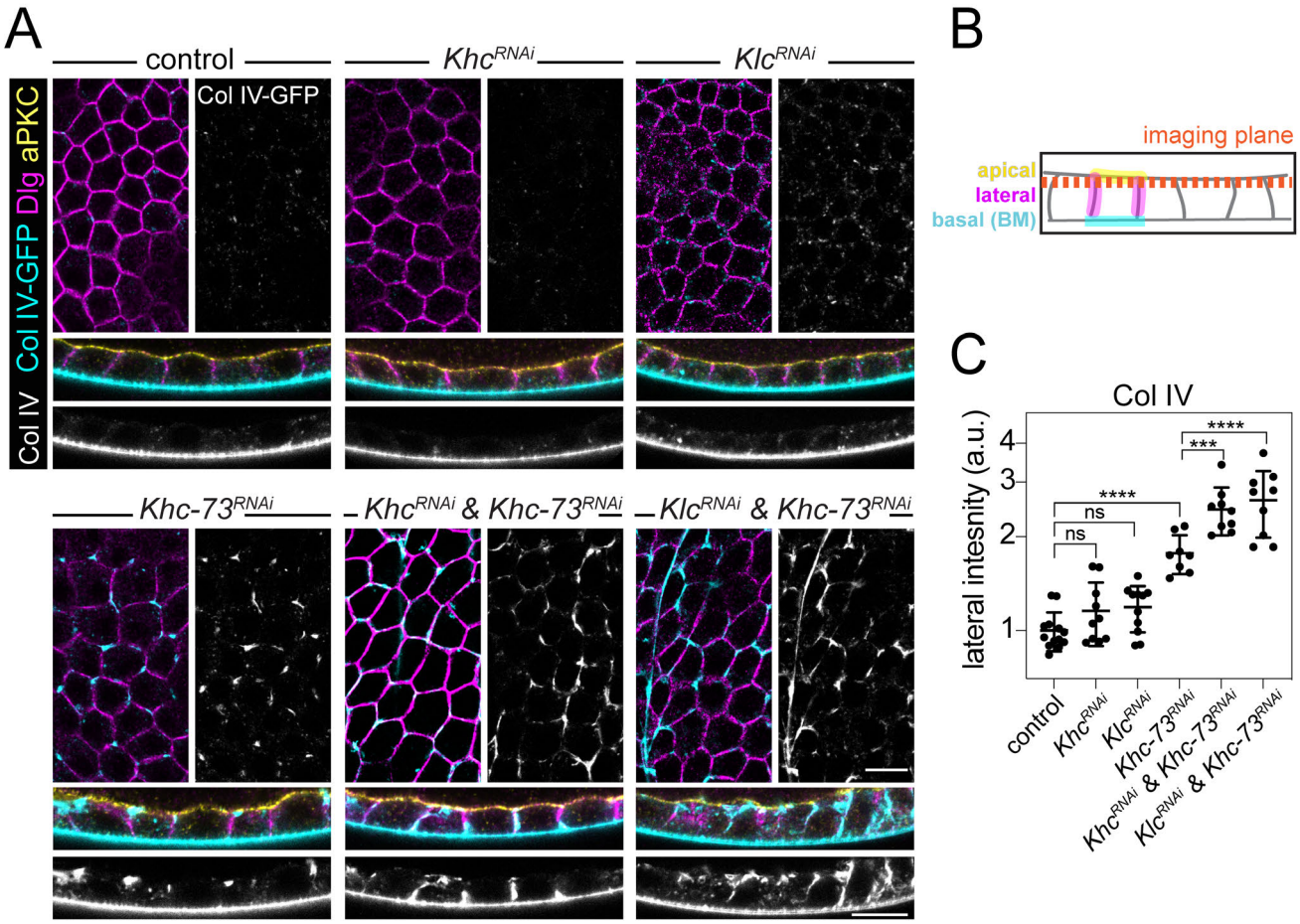

Figure 5. The kinesin-1 Khc works with Khc-73 to direct polarized BM protein secretion

520

521 **Figure 5. The kinesin-1 Khc works with Khc-73 to direct polarized BM protein secretion**

522 A. Images showing ectopic Col IV-GFP accumulation in epithelia expressing RNAi against Khc,
523 Klc, Khc-73, and combinations thereof. Top panels are planes through the lateral domains that
524 capture some of the apical surface due to tissue curvature, as diagrammed in (B). Bottom
525 panels are cross sections. Anti-Dlg marks lateral domains. Anti-aPKC marks apical domains
526 (only shown in cross sections).

527 B. Illustration of imaging planes in (A).

528 C. Quantification of ectopic Col IV-GFP accumulation at lateral cell edges in the plane used in (A)
529 for all RNAi conditions. Data represent mean ± SD plotted on a log scale. Ordinary one-way
530 ANOVA with Holm-Šídák's multiple comparisons test; ns $p>0.05$, ***$p<0.0005$, ****$p<0.0001$. In
531 the order on graph, n=13, 10, 11, 8, 9, 9 egg chambers.

532 Stage 8 egg chambers. Scale bars, 10 μm. See also Figure S5A and S5B.

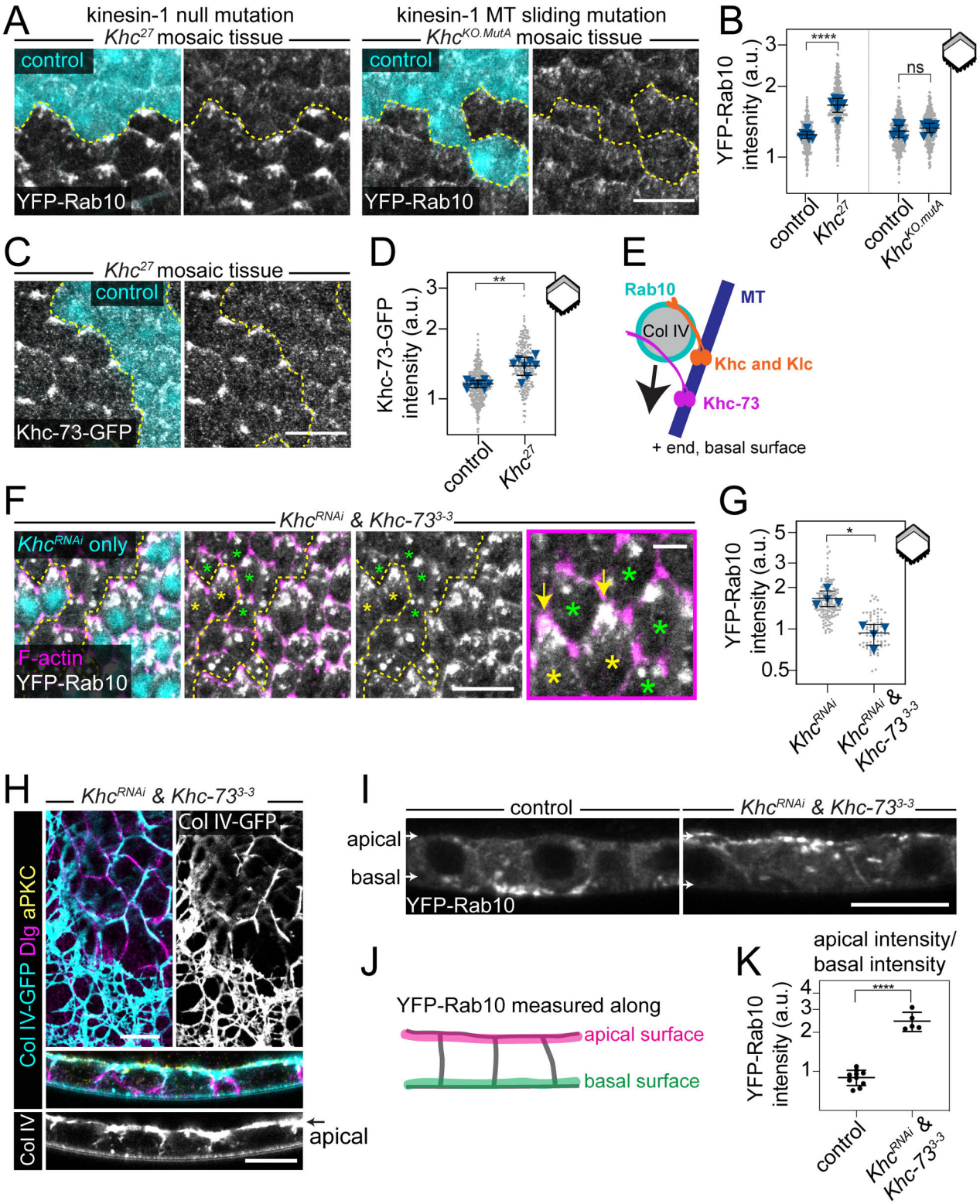

Figure 6. Khc contributes to the transport of Rab10+ compartments to the basal surface

533

Figure 6. Khc contributes to the transport of Rab10+ compartments to the basal surface

A. Image of YFP-Rab10 (endogenous) along the basal surface in *Khc*^{27} and *Khc*$^{KO.mutA}$ mosaic tissues. The dotted line demarcates control and mutant cells.

B. Quantification of the increase in YFP-Rab10 (endogenous) at the basal trailing edge (grey region of cell in cartoon) of *Khc*^{27} cells, with no change in *Khc*$^{KO.mutA}$ cells. Grey dots represent individual cells and blue triangles represent egg chamber means. Paired t tests, ns $p>0.05$, ****$p<0.0001$. For *Khc*^{27}, n=8 egg chambers, 351 control and 339 mutant cells. For *Khc*$^{KO.mutA}$, n=8 egg chambers, 344 control and 366 mutant cells.

C. Image of Khc-73-GFP (endogenous promoter) along the basal surface in *Khc*^{27} mosaic tissue. The dotted line demarcates control and *Khc*^{27} cells.

D. Quantification of the increase in Khc-73-GFP (endogenous promoter) at the basal trailing edge (grey region of cell in cartoon) of *Khc*^{27} cells. Grey dots represent individual cells and blue triangles represent egg chamber means. Paired t test, **$p<0.01$. n=8 egg chambers, 372 control and 245 *Khc*^{27} cells.

E. Model for two kinesins' role in transporting BM protein secretory vesicles.

F. Image of UAS-YFP-Rab10 along the basal surface in *Khc*^{RNAi} & *Khc-73*$^{3-3}$ mosaic tissue. The dotted line demarcates the *Khc*^{RNAi} only and *Khc*^{RNAi} & *Khc-73*$^{3-3}$ cells. F-actin is shown to visualize cell edges. Yellow asterisks mark two *Khc*^{RNAi} only cells and green asterisks mark the *Khc*^{RNAi} & *Khc-73*$^{3-3}$ cells enlarged in inset (magenta outline) to highlight higher YFP-Rab10 accumulation at trailing edges (arrows) of *Khc*^{RNAi} only cells.

G. Quantification of the decrease in UAS-YFP-Rab10 in *Khc*^{RNAi} & *Khc-73*$^{3-3}$ cells relative to *Khc*^{RNAi} only cells at basal trailing edges (grey region of cell in cartoon). Grey dots represent individual cells and blue triangles represent egg chamber means. Paired t test, *$p<0.05$. n=4 egg chambers, 153 *Khc*^{RNAi} only and 79 *Khc*^{RNAi} & *Khc-73*$^{3-3}$ cells.

H. Images of the ectopic apical Col IV-GFP network formed in a *Khc*^{RNAi} & *Khc-73*$^{3-3}$ epithelium. Top panel is a plane through the lateral domains that captures some of the apical surface due to tissue curvature. Bottom panel is a cross section. Anti-Dlg marks lateral domains. Anti-aPKC marks apical domains (only shown in cross sections). Same imaging and display settings as Figure 5A.

I. Images of UAS-YFP-Rab10 in cross-sections through control and *Khc*^{RNAi} & *Khc-73*$^{3-3}$ epithelia. In control, UAS-YFP-Rab10 at the basal surface is only visible where the cross-section passes though the trailing edge of a cell. Apical UAS-YFP-Rab10 is uniformly along the apical surface in mutant.

J. Illustration of where YFP-Rab10 intensity was measured in (I).

K. Quantification of the apical surface enrichment of UAS-YFP-Rab10 in *Khc*^{RNAi} & *Khc-73*$^{3-3}$ epithelia, measured along the surfaces illustrated in (J). Data represent mean ± SD and are plotted on a log scale. Unpaired t test, ****$p<0.0001$. n=10 control and 5 *Khc*^{RNAi} & *Khc-73*$^{3-3}$ egg chambers.

Stage 7 egg chambers (A-G). Stage 8 egg chambers (H-K). Data represent mean ± SD and are plotted on a log scale (B,D,G). Statistics are performed on egg chamber means. Scale bars 10 μm, except inset in F which is 2 μm. See also Figures S5C-E and S6.

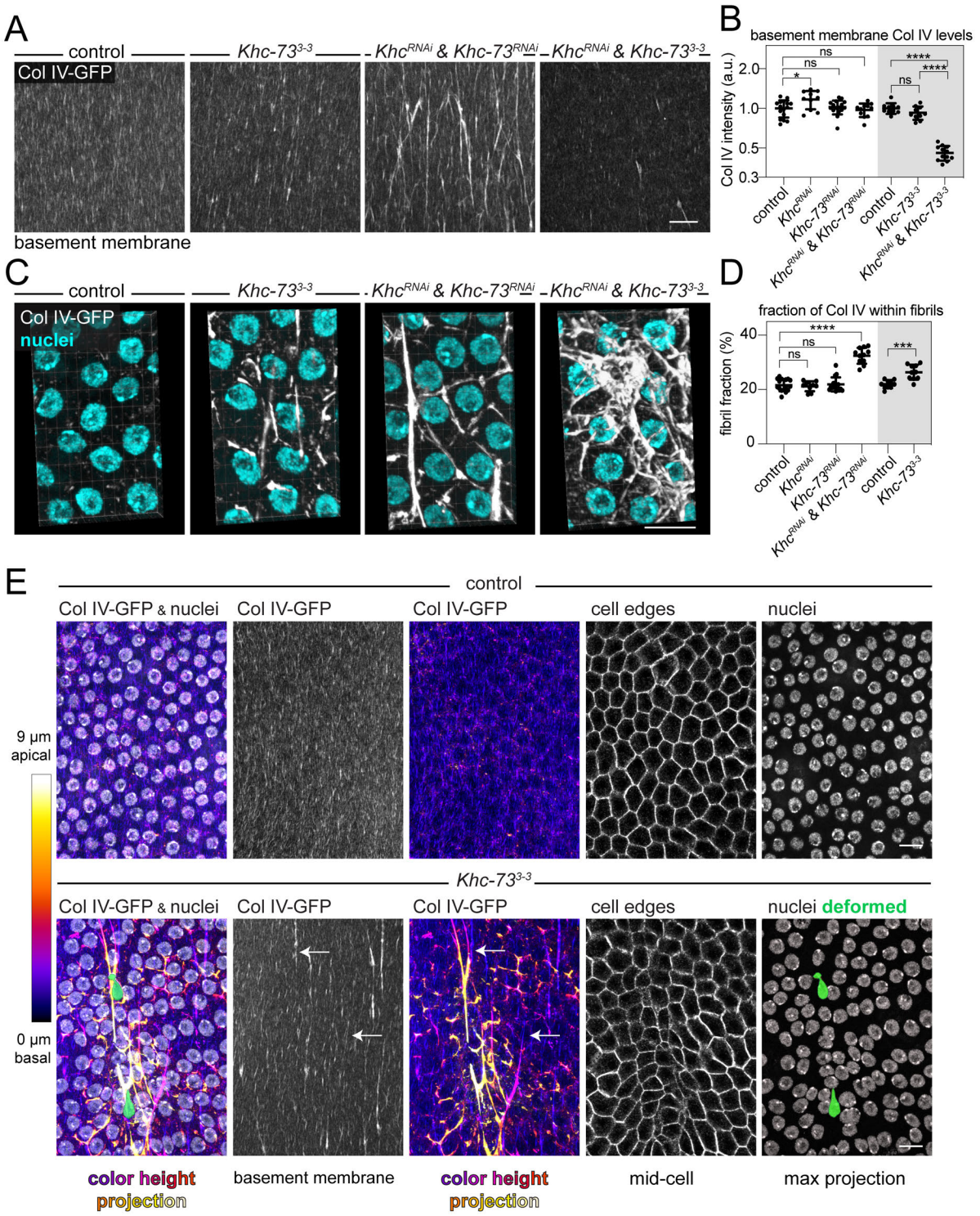

Figure 7. Intercellular BM protein networks disrupt epithelial architecture

575

576 **Figure 7. Intercellular BM protein networks disrupt epithelial architecture**

577 A. Images showing changes in the organization, and intensity, of Col IV-GFP within the BMs of
578 kinesin mutant egg chambers.

579 B. Quantification of mean Col IV-GFP intensity in the BMs from (A). Ordinary one-way ANOVA with
580 Šídák's multiple comparisons test; ns $p>0.05$, *$p<0.05$, ****$p<0.0001$. In order on graph,
581 n=16,10,16,11,10,10,12 egg chambers.

582 C. 3D projection of Col IV-GFP intercellular networks formed in a *Khc-73*$^{3-3}$ epithelium and a *Khc-*
583 *73*^{RNAi} & *Khc*^{RNAi} epithelium. An apical web-like network is formed in a *Khc*^{RNAi} & *Khc-73*$^{3-3}$
584 epithelium. The planes containing the basal sheet of BM were removed before making
585 projection. The view shown is looking down onto the apical surfaces of follicle cells.

586 D. Quantification of the fraction of Col IV-GFP intensity associated with BM fibrils in (A). One-way
587 ANOVA followed by Dunn's multiple comparison test, ns $p>0.05$, ****$p<0.0001$. For control and
588 *Khc-73*$^{3-3}$ (grey region of graph), unpaired t test, ***$p<0.0005$. In order on graph,
589 n=16,9,16,11,10,10 egg chambers.

590 E. Images showing the effect of Col IV-GFP intercellular cables on cell and nuclear shapes. A color
591 height projection of Col IV-GFP from a confocal volume of the full-thickness of the follicle cells
592 shows ectopic cables of Col IV-GFP pass through the region where cells and nuclei are
593 deformed. Arrows indicate where intercellular Col IV cables contact the underlying BM. Images
594 oriented such that migration is down. See also Movie 6

595 Stage 8 egg chambers. Data represent mean ± SD and are plotted on a log scale. Scale bars 10 μm.

596 **METHODS**
597
598 **RESOURCE AVAILABILTY**
599 ***Lead Contact***
600 Further information and requests for resources and reagents should be directed to and will be fulfilled
601 by the Lead Contact, Sally Horne-Badovinac (shorne@uchicago.edu).
602
603 ***Materials Availability***
604 New *Drosophila* lines and plasmids generated in this study are available by request to the Lead Contact
605 above.
606
607 ***Data and Code Availability***
608 Sequence data is included in Supplemental Table 3. This study did not generate new code.
609
610 **EXPERIMENTAL MODEL AND SUBJECT DETAILS**
611 ***Drosophila* care**
612 *Drosophila melanogaster* were reared on cornmeal molasses agar food at 25°C using standard
613 techniques. The genotypes used in each experiment are listed in Supplemental Table 1. Females were
614 aged on yeast with males prior to dissection; temperatures and yeasting conditions used for each
615 experiment are in Supplemental Table 2 indexed by figure.
616
617 **METHOD DETAILS**
618 **Generation of *Khc-73$^{3-3}$* allele**
619 Clustered regularly interspaced short palindromic repeats (CRISPR) genome editing was used to
620 induce a lesion near the amino-terminus of Khc-73 within the motor domain. Two guide RNAs were
621 selected using *Drosophila* RNAi Screening Center's "Find CRISPRs" on-line tool, one within exon 3 (5'
622 ATATGCACGCATTATAGCCC**TGG** 3') and one within exon 4 (5' CTTGTACATAAGCTCGGGTG**TGG**
623 3'). The PAM motifs are in bold, and the underlined sequences were cloned into pU6-BbsI-chiRNA
624 following the methods in (Gratz et al., 2013, 2014) and the website flycrispr.org. *GenetiVision* injected
625 chiRNA plasmids into embryos expressing nanos-Cas9 from the x chromosome. Individual lines were
626 established and screened by PCR and sequencing. The *Khc-73$^{3-3}$* allele has a lesion near the guide site
627 in exon3 only that results in a stop codon. The sequence of the resulting lesion, primers, and all
628 plasmid sequences are available in Supplemental Table 3. We focus on developmental stages 7 and 8
629 in this mutant because there are not obvious defects in BM protein secretion earlier in development

630 with loss of only Khc-73. BM protein secretion is highest at stage 7 which could make it easier to detect
631 secretion defects, but we cannot rule out developmental changes in secretion regulation.
632
633 **Egg chamber dissections**
634 Ovaries were removed from yeasted females using 1 set of Dumont #55 forceps and 1 set of Dumont
635 #5 forceps in live cell imaging media in a spot plate (Schneider's *Drosophila* medium containing 1X
636 Penicillin-Streptomycin, 15% fetal bovine serum, and 200 µg/ml insulin). Ovariole strands were
637 mechanically removed from muscle with forceps. Egg chambers older than stage 9 were cut away from
638 the ovariole strand in the stalk region using a 27-gauge needle. For additional methods and videos of
639 dissection, see (Cetera et al., 2016).
640
641 **Live imaging sample preparation**
642 For live imaging, dissected ovarioles were quickly moved to a fresh well of live imaging media in a spot
643 plate. In some live experiments, noted in the appropriate sections, CellMask™ Orange or Deep Red
644 plasma membrane stain was used to visualize cell edges and aid in imaging setup. Either version of
645 CellMask™ was added at 1:2000 to ovarioles in live imaging media for 15 min. The ovarioles were then
646 washed 2x in fresh live imaging media to remove excess stain. To make a live imaging slide, 1-5
647 ovarioles were transferred to a glass slide in 10 µl of live imaging media. Glass beads (between 10 and
648 50) with a mean diameter of 51 µm were added for use as spacers, and arranged around the egg
649 chambers using an eyelash tool. A 10 µl drop of fresh live imaging media was added to a #1.5 22x22
650 mm square cover glass to prevent bubbles, and slowly lowered onto the egg chambers. The slide was
651 sealed with melted petroleum jelly before imaging. New dissections were done every hour to avoid
652 artifacts arising from extended *ex vivo* culture.
653
654 **Extracellular stain of Col IV-GFP**
655 Egg chambers were fixed for 6 min at room temperature (RT) in 4% EM grade formaldehyde in
656 phosphate buffer saline (PBS), washed 3x5 min in PBS at RT, and stained with 1:2000 anti-GFP
657 nanobody conjugated to Alexa Fluor® 647 (GFP-Booster) and 4′,6-diamidino-2-phenylindole (DAPI) for
658 15 min at RT with rocking *without* permeabilization to allow the nanobody access to only the
659 extracellular pool of Col IV-GFP. Samples were washed 3x5 min with PBS.
660
661 **Immunostaining**
662 Egg chambers were fixed in 4% EM-grade formaldehyde in PBS with 0.1% Triton X-100 (PBST) for
663 permeabilization for 15 min at room temperature, and then washed 3x10 min in PBST. For microtubule

664 (MT) staining, 8% formaldehyde in PBST was used to better preserve MTs (Doerflinger et al., 2003).
665 Egg chambers were incubated with primary antibodies diluted in PBST overnight at 4ºC with rocking.
666 Primary antibody dilutions: aPKC (1:100), Dlg (1:10), Tango1 (1:1000), GM130 (1:500), anti-acetylated
667 α-tubulin (1:100). Egg chambers were washed from primary antibody 3x10 min in PBST with rocking at
668 RT. Secondary antibodies were diluted 1:500 in PBST and incubated with egg chambers for 3 hrs at RT
669 with rocking, followed by washing 3x10 min in PBST.
670
671 **smiFISH**
672 Single molecule inexpensive fluorescent in situ hybridization (smiFISH) was based on (Tsanov et al.,
673 2016) and protocols provided by Matt Ronshaugen's lab. In this technique, DNA probes specific to the
674 mRNA of interest are fused to a "flap" sequence that will anneal to a complementary, fluorescently-
675 labeled "flap" sequence to allow visualization of the mRNA.
676 *Probe Design and Annealing*
677 DNA probes specific to *col41a* mRNA (based on cDNA clone RE33133) were designed using LGC
678 Biosearch Technologies' Stellaris® RNA FISH Probe Designer with the following settings: probe length
679 20 bases, masking level 5, minimal spacing 2 bases. 48 probes were ordered for *col4a1*. Each probe
680 contained 20 nucleotides complementary to mRNA for *col4a1* followed by Flap-X
681 (5'CCTCCTAAGTTTCGAGCTGGACTCAGTG 3') appended to the 3' end. Probes were ordered from
682 Integrated DNA Technologies (IDT) as 100 µM stocks in Tris-EDTA, pH 8.0 (TE) in a 96-well plate.
683 Probes were mixed at equal molar ratios to make a stock of unlabeled probes and stored at -20°C.
684 Working stocks were diluted 5-fold in TE buffer before use. Fluorescently labeled Flap-X binding probes
685 were ordered from IDT as DNA oligos with 5' and 3' Cy5 modifications and resuspended in TE at 100
686 µM. All probe sequences are listed in Supplemental Table 3. *Col4a1* probes and fluorescent probes
687 were annealed immediately before use by mixing: 2 µl of probe set, 0.5 µl of 100 µM Cy5-FlapX, 1 µl of
688 New England Biolabs® Buffer 3, and 6.5 µl water. A PCR machine was used to incubate mixtures at
689 85°C for 3 min, 65°C for 3 min, and 25°C for 5 min.
690 *Hybridization*
691 Egg chambers were fixed in 4% EM-grade formaldehyde in PBST for 15 min at room temperature (RT)
692 and washed 3x5 min in PBST. Egg chambers were exchanged into a 1:1 mixture of PBST and smiFISH
693 wash buffer [5 ml 20X SSC (0.3M sodium citrate, 3M NaCl, pH7.0), 5 ml deionized formamide, 40 ml
694 nuclease-free water] and incubated at RT for 10 min. Egg chambers were washed 2x in smiFISH wash
695 buffer, followed by a final incubation of 30 min at 37°C. smiFISH hybridization buffer (1 g dextran
696 sulfate, 1 ml 20x SSC, 1 ml deinionzed formamide, 7.5 ml nuclease-free water) was warmed to 37°C.
697 Egg chambers were incubated with a mixture of 10 µl of annealed probes in 500 µl of smiFISH

698 hybridization buffer at 37°C for 16 hrs protected from light. To wash, 500 µl of smiFISH wash buffer was
699 added to dilute hybridization buffer and the egg chambers were spun briefly in a table-top micro-
700 centrifuge to pellet them. Egg chambers were washed 3x10 min at 37°C in 500 µl of smiFISH wash
701 buffer. This was followed by incubating at RT in a 1:1 dilution of smiFISH wash buffer with PBST,
702 followed by one 10 min incubation in PBST containing DAPI and Alexa Fluor™ 488 Phalloidin, followed
703 by 2x10 min washes with PBST at RT.
704
705 **Mounting fixed samples**
706 For all types of fixed samples, the majority of buffer was removed from samples and they were
707 mounted in ~35 µl SlowFade™ antifade or VECTASHIELD® on a slide with a #1.5 22x50 mm coverslip,
708 sealed with nail polish, and stored at 4°C prior to imaging.
709
710 **Microscopy**
711 *Fixed and live laser scanning confocal imaging*
712 Imaging was performed on a Zeiss LSM 800 laser scanning confocal microscope with Zen blue, 63x
713 Plan A apochromat 1.4NA oil objective. Live imaging was performed at RT. Used in Figures 1A, 1D, 2A,
714 2C, 3A, 4A, 4C, 5A, 6A, 6C, 6F, 6H, 6I, 7A, 7C, 7E, S1B, S1D, S1F, S2A, S2B, S3A, S3F, S4A, S4B,
715 S5A, S6A, S6B, Movie 1, and Movie 6.
716 *Airyscan fixed imaging*
717 Zeiss LSM 880 laser scanning confocal microscope with Airyscan and a 63x Plan A apochromat 1.4NA
718 oil objective run by Zen black. Used in Figures 3D, 3E, and Movie 2.
719 *Live spinning disk confocal and partial TIRF imaging*
720 Imaging was performed on a Nikon Ti-E inverted microscope equipped with solid-state 50 mW, 481 and
721 561 nm Sapphire lasers (Coherent), a Yokogawa CSU-X1 spinning-disk scan head, and an Andor
722 iXon3 897 electron-multiplying charged-coupled device (EM-CCD) cameras run by MetaMorph
723 software. When using the TIRF microscope, we adjusted the laser below the critical angle to illuminate
724 a thicker region of the sample (partial TIRF). Live imaging was performed at RT. Spinning disk used in
725 Figure 3G and Movie 3. Partial TIRF used in Figures 3C, 4F, S3C, S5C, S6E, Movie 4, and Movie 5.
726
727 **Quantification of lateral BM proteins**
728 Single confocal images were taken in a plane through the lateral domains, near the apical surfaces of
729 follicle cells from late stage 8 egg chambers when new Col IV-GFP synthesis is low and ectopic lateral
730 Col IV-GFP in mutant egg chambers is easily visible. The average intensity of Col IV-GFP associated
731 with lateral domains was measured by segmenting the lateral domains based on anti-Dlg staining. In

732 Fiji, Dlg images were processed as follows: background was subtracted with Rolling Ball Background
733 Subtraction with a radius of 10 pixels, Threshold was used to create a binary mask, Despeckle was
734 used to remove noise, Dilate was used to fill in gaps in the lateral edges, Skeletonize was used to
735 reduce the mask to a one pixel outline, and finally Dilate was used to reach a uniform line thickness of
736 0.7 μm. This binary mask was used to measure the mean intensity of Col IV-GFP within only the lateral
737 regions. In some images, the Dlg staining quality was too noisy for automatic segmentation, and the
738 cell edges were manually traced in Fiji and converted to the same thickness as the automatic
739 segmentation. For LanA-GFP and Perlecan-GFP, samples were counterstained with Alexa Fluor™ 647
740 Phalloidin, not anti-Dlg. F-actin highlights the cell edges, which were manually traced in Fiji and then
741 converted to the same thickness as the automatic segmentation. The data were normalized to the
742 mean of the control egg chambers for easy comparison as fold-change relative to control.
743

744 **Quantification of extracellular lateral Col IV-GFP**

745 Additional processing was required for lateral extracellular Col IV-GFP because the "near basal" plane
746 is near the BM, which creates high background fluorescence. Extracellular Col IV staining is necessary
747 during stages when new Col IV protein synthesis is high (stage 7 in these experiments) and Col IV-GFP
748 foci are scattered throughout the cytoplasm, obscuring the secreted, lateral Col IV-GFP population.
749 Three planes were chosen from a confocal z-stack of mosaic *Khc-73*$^{3-3}$ tissue for analysis: a plane
750 "near basal", or about 1 μm above the BM, a plane through the middle of the cell ("mid-cell"), and a
751 plane just below the apical surface of cells ("near-apical"). The lateral cell edges were manually traced
752 in Fiji with a line thickness of 1.12 μm at each z-plane. The mean intensity of the anti-GFP nanobody
753 staining (extracellular Col IV-GFP, see Figure S1F) was measured in the segmented lateral regions for
754 both the control and *Khc-73*$^{3-3}$ cell regions. The mean intensity was also measured in the inverse
755 regions, within the cell centers where there should not be any extracellular staining; the mean intensity
756 in these cell center regions was used for background subtraction in each plane, which is particularly
757 important for the images near the basal surface where the out of focus fluorescence from the BM
758 generates high background. The background corrected mean lateral intensity is calculated: mean
759 intensity lateral regions – mean intensity central regions. To allow the data to be read as fold change
760 between control and *Khc-73*$^{3-3}$ cells in one egg chamber, and be compared across z-planes, all data
761 was divided by the mean of the control cells in the "near basal" images for each egg chamber.
762

763 **Line-scans of β-catenin and Col IV-GFP**

764 Confocal images of cross-sections through *Khc-73*$^{3-3}$ egg chambers expressing Col IV-GFP and
765 stained for anti- β-catenin were taken. In Fiji, lines of 0.58 μm thickness were manually drawn along 20

766 cell-cell junctions containing ectopic lateral Col IV-GFP, starting above the apical surface and extending
767 along the lateral domain. The average intensities of Col IV-GFP and β-catenin were measured along
768 the line-scan using Plot Profile and exported to Microsoft Excel. The maximum intensity of β-catenin
769 was used to determine the location of the zonula adherens and used as a comparison point to align all
770 the traces, where the zonula adherens was set to a distance of zero. All individual traces for Col IV-
771 GFP intensity were plotted to show the range of accumulation patterns. B-catenin is drawn as a line at
772 zero as it is used only as a reference point for the zonula adherens junction that demarcates the lateral
773 and apical domains.
774
775 **Colocalization of Col IV-GFP and the ER**
776 Egg chambers expressing UAS-RFP-KDEL as a luminal marker of the ER and Col IV-GFP were
777 dissected and stained with CellMask^{TM} Deep Red as described. Egg chambers were imaged live to
778 better preserve ER structure. For the images shown, three consecutive frames from a time-lapse taken
779 1 sec apart were averaged to decrease noise.
780
781 **Quantification of YFP-Rab10**
782 *At basal trailing cell edges*
783 Images were taken along the basal surface of cells in mosaic tissues. YFP-Rab10 is present as a
784 diffuse cytoplasmic signal as well as a more intense signal on punctae and tubules at basal trailing cell
785 edges, likely representing the vesicular structures of interest. To focus our measurements on the YFP-
786 Rab10 associated with these putative vesicular structures, we quantified YFP-Rab10 intensity changes
787 in only basal trailing cell edges so that the mean YFP-Rab10 measurements would not be dominated
788 by the cytoplasmic signal that covers a much larger area of cells. In Fiji, a line with a thickness of 1.2
789 μm was manually drawn along the back of each cell and the mean YFP-Rab10 intensity was measured
790 in each cell. To normalize the YFP-Rab10 intensities across egg chambers, the entire control cell area
791 was manually segmented in Fiji and the mean YFP-Rab10 intensity measured. All individual cell values
792 were divided by this value. In addition to individual cell measurements, we also calculated the mean of
793 all cells per genotype for each egg chamber. Statistical tests were performed using these mean egg
794 chamber values, but all individual cells are also plotted to show the variability in the underlying data
795 (Lord et al., 2020).
796 *Near the ERES*
797 YFP-Rab10 is localized near ERES/Golgi regions throughout the volume of the cells. Near the basal
798 surface, the tubules at the backs of cells are brighter than the signal by the Golgi, and their close, and
799 sometimes overlapping, signal makes it difficult to measure the levels of YFP-Rab10 near ERES/Golgi.

800 In the middle of the cells, the majority of the YFP-Rab10 is concentrated near the ERES/Golgi so we
801 chose this plane to allow easier segmentation. Tango1 staining at the ERES was used to segment
802 these regions with the following steps: Rolling Ball Background Subtraction with radius 10 pixels was
803 used, Threshold was used to create a binary mask of the ERES, and noise was removed by running
804 Despeckle 2x in Fiji. The ERES was expanded using Dilate 2x so it would encompass the region
805 adjacent to the ERES where Rab10 is normally found. The mean intensity of YFP-Rab10 within these
806 ERES masks was measured in both the control cells and *Khc-73*$^{3-3}$ cells in each mosaic egg chamber,
807 resulting in a single mean value per genotype per egg chamber. Since the same mosaic egg chambers
808 were also used to measure the basal trailing edge YFP-Rab10 intensity, just at different z-planes, these
809 ERES means were normalized using the same value used to normalize YFP-Rab10 at the basal trailing
810 edge between egg chambers.
811
812 **Quantification of the effect of HA-Khc-73 OE**
813 We used the *traffic jam-Gal4* (*tj-Gal4*) driver to express UAS-HA-Khc73 (Siegrist and Doe, 2005). The
814 *tj-Gal4* driver usually expresses UAS transgenes in all follicle cells, but some UAS transgenes in our
815 experience express in only a subset of cells, which we refer to as “patchy” expression in the text. We do
816 not know why UAS-HA-Khc-73 in particular expresses in this patchy way. This phenomenon has also
817 been described as variegation in expression in follicle cells, thought to stem from epigenetic changes
818 (Lee and Spradling, 2014; Lee et al., 2017; Skora and Spradling, 2010). Since we can stain for the HA
819 epitope tag, we were able to select non-expressing cells and HA-Khc-73 expressing cells. Images were
820 taken near the basal surface of tissues patchily overexpressing HA-Khc-73, which clusters at the basal
821 trailing edges of cells. To determine if HA-Khc-73 recruited other proteins to these clusters, we
822 measured intensities in 1.2 μm lines drawn along the basal trailing edges of cells, similar to the
823 procedure used to measure basal trailing edge YFP-Rab10. We chose to measure along the trailing
824 edges instead of segmenting the HA+ regions because this more general location could be selected in
825 the non-expressing cells as a control for baseline localization of candidate proteins to the trailing edge
826 of cells. Cells that were negative for HA-Khc-73 staining (“control”) or positive for HA-Khc-73 were
827 selected from within the same egg chamber. The mean intensity of the relevant endogenously tagged,
828 fluorescently labeled protein (YFP-Rab10, Col IV-GFP, PDI-GFP (ER), or anti-GM130 (cis Golgi)
829 staining) was measured for each cell. For each egg chamber, all individual cell measurements were
830 normalized by dividing by the mean value for control cells within that egg chamber. In addition to
831 individual cell measurements, we also calculated the mean of all cells per group (“control” or “HA-Khc-
832 73”) for each egg chamber. Statistical tests were performed using these mean group values, but all
833 individual cells are also plotted to show the variability in the underlying data (Lord et al., 2020).

834

835 **Live imaging YFP-Rab10 in HA-Khc-73 OE cells**

836 We used the *traffic jam-Gal4* (*tj-Gal4*) driver to express UAS-HA-Khc73 and UAS-YFP-Rab10. Images
837 were collected in a continuous 200 ms stream to follow the rapid movements of YFP-Rab10, using
838 partial TIRF.

839

840 **Live imaging and tracking of YFP-Rab10**

841 *Selection of egg chambers*

842 In some experiments, CellMask™ Orange plasma membrane stain was used to visualize cell edges. To
843 ensure egg chambers were not damaged during dissection or sample preparation, we first determined if
844 they were migrating at a normal rate. A 5-30 min time-lapse using 300 ms exposures taken every 15
845 sec was taken for each egg chamber to ensure it was migrating at a normal speed (a cutoff of > 0.4
846 μm/min was set for the stage 7 egg chambers used). Sets of control and *Khc-73*$^{3-3}$ egg chambers were
847 always imaged in the same session to prevent biases from day-to-day variability in live imaging
848 conditions. Since partial TIRF imaging was used, there is uneven illumination across the field of cells.

849 *Tracking and analysis*

850 To allow tracking of rapidly moving individual YFP-Rab10 punctae, time-lapses with 300 ms exposures
851 captured every 1 sec for 2 min were made. YFP-Rab10 punctae were manually tracked using the
852 Manual Tracking plugin in Fiji. All punctae that moved at least 3 pixels (0.3 μm) per 1 sec time-step
853 over at least 3 consecutive frames were tracked in at least 5 cells per egg chamber to obtain a
854 minimum of 50 puncta tracks per egg chamber, in 5 egg chambers per genotype. We sometimes
855 observed a change in direction of a YFP-Rab10 puncta. Each segment in a single direction was
856 counted as a separate "run", allowing a single puncta to represent multiple runs. Each run was scored
857 by eye for its overall direction, either towards the trailing or leading edge of the cell. For each egg
858 chamber, the number of tracks moving towards the trailing edge of the cell was divided by the number
859 of tracks moving towards the leading edge of each cell, such that a value greater than 1 indicates a
860 bias in movement towards the trailing edge where YFP-Rab10 accumulates. In addition, the speed of
861 each "run" was calculated. Speed was calculated as the Euclidian frame-to-frame displacement. All
862 individual "run" speeds across all 5 egg chambers were plotted to compare the distributions between
863 control and *Khc-73*$^{3-3}$ cells, and the mean speed per egg chamber was also plotted and used for
864 statistical comparison between genotypes. All analysis was done on original images; for display in
865 figures, images were rotated in Fiji so that the direction of cell migration is toward the bottom of the
866 page.

867

868 *Editing of images for Movie 5*
869 For movies, images were rotated such that the direction of cell migration is toward the bottom of the
870 page. The CellMask staining channel was processed with a Rolling Ball Background subtraction, radius
871 20 in Fiji. Both the YFP-Rab10 and CellMask channels were processed with Bleach Correction in Fiji for
872 the first segment of Movie 5. The images of trajectories were generated in Fiji with the Manual Tracking
873 plug-in.
874
875 **Quantification of apical and basal YFP-Rab10 levels**
876 In images of cross-sections through egg chambers, lines of 0.6 μm thickness were manually drawn
877 along the basal surface and apical surface of the follicular epithelium of each egg chamber and the
878 mean intensity of YFP-Rab10 measured in Fiji. The ratio of the apical and basal surface values was
879 calculated for each egg chamber, such that a ratio greater than 1 indicates an enrichment of YFP-
880 Rab10 on the apical surface, and a ratio less than 1 indicates an enrichment of YFP-Rab10 on the
881 basal surface.
882
883 **Measurement of fraction of Col IV within fibrils in the BM**
884 As a way to quantify changes in the organization of Col IV-GFP within the BM, we measured the
885 fraction of Col IV-GFP intensity associated with fibril-like structures in the BMs of different genotypes.
886 We have previously performed this analysis and refer to it as “fibril fraction” (Isabella and Horne-
887 Badovinac, 2016). First, we determined if the overall mean intensity of Col IV-GFP was the same.
888 The mean intensity of Col IV-GFP in a confocal plane though the BM was measured in a square region
889 (3600 μm^2) for each egg chamber in Fiji. The genotype that causes apical secretion had significantly
890 reduced Col IV-GFP in the BM, so it was excluded from fibril fraction analysis. To segment the fibrils,
891 the median intensity of Col IV-GFP was measured for each egg chamber and a threshold of 1.35x
892 median intensity was used to define the brighter, “fibril” areas. The Col IV-GFP intensity in these “fibril”
893 regions was divided by the total Col IV-GFP intensity in the image to obtain the % of total Col IV-GFP
894 intensity associated with fibrils.
895
896 **Color 3D projections**
897 *Of MTs*
898 The temporal color-code plug-in in Fiji was used to generate a color z-projection of a 1.8 μm Airyscan
899 confocal z-stack of MTs in a wild type egg chamber. An antibody specific to acetylated MTs was used
900 for this imaging because this antibody has been used in all previous work characterizing the basal MT
901 array in follicle cells (Aurich and Dahmann, 2016; Chen et al., 2016; Viktorinová and Dahmann, 2013)

902 and we wanted to ensure we visualized the same MT array as past work. Live imaging of MTs labeled
903 with UAS-ChRFP-Tubulin or Jupiter-GFP show a similar organization of MTs at the basal surface
904 (Figures 3G, S3C, S5C, and S6E).
905 *Of intercellular BM protein network*
906 The temporal color-code plug-in in Fiji was used to generate a color z-projection of Col IV-GFP in a
907 confocal z-stack through the full-thickness of the follicle cells (9 µm). The cell outlines are Dlg staining
908 of lateral cell edges in a single plane through the middle of FCs. The nuclei are maximum intensity
909 projections of the DAPI signal from the z-stack to show the full shape of the nucleus. In the more apical
910 slices of the z-stack, the large nuclei from the germline nurse cells were visible; these were manually
911 circled and deleted from the Z-stack prior to making the maximum intensity projection. The nuclei
912 highlighted in green with deformed/elongated shapes were manually highlighted in Illustrator.
913
914 **3D projections of intercellular Col IV-GFP**
915 A 3D confocal z-stack through the full thickness of the follicle cells was collected. The slices containing
916 the BM were deleted to provide better contrast to visualize the intercellular Col IV-GFP network. 3D
917 projections were generated in Fiji using the Plugin ClearVolume.
918
919 **smiFISH quantification**
920 The density of *col4a1* mRNA precluded single-molecule counting. We used the intensity of the smiFISH
921 probes as a proxy for mRNA levels. Three z-planes through the lateral domains of the follicle cells were
922 chosen for analysis in each egg chamber to determine if the localization of mRNA changed in mutant
923 cells: a plane along the basal surface, a plane through the mid-section of the cells, and a plane near the
924 apical surface. Within the mosaic tissue, regions encompassing cells of different genotypes were
925 manually drawn based on the nuclear clone marker in Fiji. The mean intensity of *col4a1* mRNA was
926 measured for each genotype at each plane. Intensities between genotypes within mosaic tissues were
927 compared within the same egg chamber at each plane by: dividing $Khc\text{-}73^{3\text{-}3}$ cells by control cells, or
928 dividing Khc^{RNAi} & $Khc\text{-}73^{3\text{-}3}$ cells by Khc^{RNAi} only cells. The direction of follicle cell migration (to orient
929 images) was determined by the organization of F-actin rich leading edges along the basal surface
930 visualized by counter-staining egg chambers with Alexa Fluor™ 488 Phalloidin.
931
932 **Quantification of Patronin-GFP**
933 Egg chambers were fixed and stained with Alexa Fluor™ 647 Phalloidin and DAPI. Confocal cross-
934 sections were taken through egg chambers. In Fiji, a 1.1 µm thick line was manually drawn along the
935 apical surface where Patronin is normally enriched (Khanal et al., 2016; Nashchekin et al., 2016), using

the F-actin stain to visualize cell outlines. The mean apical intensity of Ubi-PatroninA-GFP in *Khc-73*$^{3-3}$ cells was divided by that of control cells in each egg chamber, resulting in a ratio of 1 when there is no change.

Quantification of Jupiter-GFP

Intensity in cross-section

Confocal cross-sections were taken through live egg chambers stained with CellMask™ Deep Red plasma membrane stain to aid in setting up imaging and identifying the borders of cells. In Fiji, the control and *Khc-73*$^{3-3}$ cells were manually outlined based on the clone marker, and the mean intensity of endogenously-tagged Jupiter-GFP (a MT-associated protein) was measured as a proxy for MT mass. The mean Jupiter-GFP intensity in *Khc-73*$^{3-3}$ cells was divided by that of the control cells in each egg chamber.

Basal MT alignment

Partial TIRF images of the basal surface of live mosaic egg chambers expressing Jupiter-GFP were taken. First, a 5-30 min time-lapse was collected to determine the direction of migration and to exclude non-migratory egg chambers damaged during dissection. To quantify MT alignment, we used an approach based on the Sobel operator (Gonzalez and Woods, 2017) to identify the sharp local gradients in fluorescent intensity present orthogonal to linear structures like MTs, as implemented in (Li and Munro, 2020). Images of Jupiter-GFP were convolved with the following 3x3 kernel Sobel operators to measure the x and y components of the fluorescent intensity gradient (Gx and Gy, respectively).

$$Gx = \begin{matrix} 1 & 2 & 1 \\ 0 & 0 & 0 \\ -1 & -2 & -1 \end{matrix} \quad \text{and} \quad Gy = \begin{matrix} 1 & 0 & -1 \\ 2 & 0 & -2 \\ 1 & 0 & -1 \end{matrix}$$

For each pixel, the angle and magnitude of the gradient can be calculated using the x and y components of the gradient. Since the gradient is orthogonal to the angle of the MT, the angle of the MTs θ is

$$\theta = \tan^{-1}\frac{Gy}{Gx}$$

And the magnitude of the gradient, G, is

$$G = \sqrt{Gx^2 + Gy^2}$$

To create MT alignment distributions, regions of cells with different genotypes were manually outlined in Fiji based on the clone marker. The pixels within regions of a given genotype were binned by angle with weight G, collapsed to 0º-90º since we do not take into account angle relative to the A-P axis, and then normalized to 100%. The mean ± SD at each angle bin of all egg chambers of a given genotype were plotted on a rose diagram, where perfect alignment with the direction of migration would be 90º and alignment orthogonal to migration would be 0º. To statistically compare the amount of alignment between genotypes, the % of the alignment histogram within angles 60º-90º was used as proxy measurement of the population of "highly aligned MTs". This "% highly aligned MTs" measurement was performed for each genotype in each egg chamber. All analysis was done on original images; for display in figures, images were rotated so that the direction of cell migration is toward the bottom of the page. MT intensity appears uneven across the egg chamber because these images were collected with partial TIRF which creates an uneven illumination depth and some interference patterns across the imaging field.

Generation of Movies

Fiji was used to add labels and export movies as .avi, which were then converted to .mp4 using HandBrake.

QUANTIFICATION AND STATISTICAL ANALYSIS

Egg chambers with visible damage from dissection or dying cells, or not migrating at a normal speed in live imaging experiments, were excluded. All experiments were replicated at least once. All statistical tests were performed in Prism8 or Prism9. MATLAB® and Microsoft Excel were used as indicated in Methods for some data analysis. All data was tested for normality using the Shapiro-Wilks test and a non-parametric statistical test was chosen if a dataset was not normal. For comparisons between cells with different genetic perturbations within a mosaic tissue, a paired statistical test was chosen. When experiments compared data taken from different egg chambers, unpaired statistical tests were used. ANOVA followed by a multiple comparisons test was used for comparison of more than two datasets. Many experiments compare the ratio between mutant and control cells, which would result in a value of 1 if there was no difference between groups; in these experiments a one-sample t test or the non-parametric Wilcoxon signed rank test was used to compare the experimental ratio to the theoretical

999 value of 1. The number of biological replicates (n), specific statistical tests performed, and significance
1000 for each experiment can be found in the figure legends.

1001 **RESOURCE TABLE**

REAGENT or RESOURCE	SOURCE	IDENTIFIER
Antibodies		
anti-Discs large	Developmental Studies Hybridoma Bank	Cat# DHSB: 4F3; RRID: AB_528203
anti-aPKC	Santa Cruz Biotechnology	Cat# sc-216; RRID:AB_2300359
anti-Armadillo (β-catenin)	Developmental Studies Hybridoma Bank	Cat# DHSB: N2 7A1; RRID: AB_528089
GFP-Booster Alexa Fluor™ 647	ChromoTek	Cat# gb2AF647-50; RRID AB_2827575
Anti-acetylated α-Tubulin (6-11B-1)	Santa Cruz Biotechnology	Cat# sc-23950; RRID:AB_628409
Anti-Notch	Developmental Studies Hybridoma Bank	Cat# DHSB: C458.2H; RRID: AB_528408
anti-Fasciclin III	Developmental Studies Hybridoma Bank	Cat# DHSB: 7G10; RRID: AB_528238
Anti-Tango1	Lerner et al., 2013.	
Anti-GM130 (Drosophila)	Abcam	Cat# ab30637; RRID:AB_732675
Rabbit polyclonal anti-HA	Rockland Inc.	Cat# 600-401-384; RRID: AB_218007
Alexa Fluor™ 555, donkey anti-mouse secondary	Thermo Fisher Scientific	Cat# A31570; RRID: AB_2536180
Alexa Fluor™ 647, donkey anti-mouse secondary	Thermo Fisher Scientific	Cat# A31571; RRID: AB_162542
Alexa Fluor™ 555, donkey anti-rabbit secondary	Thermo Fisher Scientific	Cat# A-31572; RRID: AB_162543
Alexa Fluor™ 647, donkey anti-rabbit secondary	Thermo Fisher Scientific	Cat# A31573; RRID: AB_2536183
Alexa Fluor™ 647, goat anti-guinea pig secondary	Thermo Fisher Scientific	Cat# A-21450; RRID: AB_2735091
Chemicals, Peptides, and Recombinant Proteins		
Alexa Fluor™ 647 phalloidin	Thermo Fisher Scientific	Cat# A22287
CellMask™ Deep Red Plasma Membrane Stain	Thermo Fisher Scientific	Cat# C10046
CellMask™ Orange Plasma Membrane Stain	Thermo Fisher Scientific	Cat# C10045

Schneider's Drosophila Medium	Thermo Fisher Scientific	Cat# 21720-024
Fetal Bovine Serum	Gibco	Cat# 10438-018
Recombinant Human Insulin	Millipore Sigma	Cat# 12643
Soda Lime Glass Beads, 48-51 µm	Cospheric LLC	Cat# S-SLGMS-2.5
Formaldehyde, 16%, methanol free, Ultra Pure	Polysciences	Cat# 18814-10
VECTASHIELD® Antifade Mounting Medium	Vector Laboratories	Cat# H-1000-10
SlowFade™ Antifade Kit	Thermo Fisher Scientific	Cat# S2828
Experimental Models: Organisms/Strains		
D. melanogaster. Standard control strain: w[1118]	Bloomington Drosophila Stock Center	BDSC: 3605; FlyBase ID: FBst0003605
D. melanogaster. *traffic jam-Gal4:* y* w*; P{w+mW.hs = GawB}NP1624/CyO, P{w- = UAS-lacZ.UW14}UW14	Kyoto Stock Center	DGRC: 104055; FlyBase ID: FBst0302922
D. melanogaster. w[1118]; P{w[+mC] = UAS-Dcr-2.D}10	Bloomington Drosophila Stock Center	BDSC: 24651; FlyBase ID: FBst0024651
D. melanogaster. P{ry[+t7.2] = hsFLP}22, w[*]}	Bloomington Drosophila Stock Center	BDSC: 8862; FlyBase ID: FBst0008862
D. melanogaster. Col IV-GFP: P{PTT-GC}vkg^{CC00791}	Laboratory of Lynn Cooley, Flytrap (Buszczak et al., 2007; Morin et al., 2001)	FlyBase ID: FBal0211825
D. melanogaster. w1118; *Khc-73* $^{3-3}$	This study	
D. melanogaster. w[*]; P{w[+mW.hs]=FRT(w[hs])}G13	Bloomington Drosophila Stock Center	BDSC: 1956
D. melanogaster. *rab10-*	Laboratory of P. Robin Hiesinger (Kohrs et al., 2020 bioRxiv.)	
D. melanogaster. *UAS-spastin*	Laboratory of Nina Tang Sherwood (Sherwood et al., 2004.)	FlyBase ID: FBal0177735
D. melanogaster. PBac{ *LanA-GFP*$^{fTR000\ 574}$.sfGFP-TVPTBF}VK00033	Vienna Drosophila Resource Collection (Sarov et al., 2016)	VDRC: 318155; FlyBase ID: FBal0339089
D. melanogaster. *Khc-73*^{RNAi}: y[1] sc[*] v[1] sev[21]; P{y[+t7.7] v[+t1.8]=TRiP.HMS01624}attP40	Bloomington Drosophila Stock Center	BDSC: 36733; FlyBase ID: FBal0266531

D. melanogaster. Perlecan-GFP: *P{PTT-GA}trolCA06698*	Laboratory of Lynn Cooley, Flytrap (Buszczak et al., 2007; Morin et al., 2001)	FlyBase ID: FBal0282690
D. melanogaster. *Khc-73*^{149}	Laboratory of A. Pejmun Haghighi (Liao et al, 2018)	FlyBase ID: FBal0344596
D. melanogaster. *hsFLP; FRTG13 Ubi-mRFP.nls/Cyo*	From the laboratory of Dan T. Bergstralh	
D. melanogaster. *traffic jam-Gal4 FRTG13 UbimRFP.nls*: w[*];P{w+mW.hs = GawB}NP1624 P{w[+mW.hs]=FRT(w[hs])}G13 P{w[+mC]=Ubi-mRFP.nls}2R	Recombination only, this study	*traffic jam-Gal4* from DGRC: 104055; *FRTG13* from BDSC: 1956; *Ubi-mRFP.nls* from BDSC: 35496
D. melanogaster. *vkg-GFP traffic jam-Gal4 FRTG13 UbimRFP.nls*: w[*];P{PTT-GC}vkg^{CC00791} P{w+mW.hs = GawB}NP1624 P{w[+mW.hs]=FRT(w[hs])}G13 P{w[+mC]=Ubi-mRFP.nls}2R	Recombination only, this study	*vkg-GFP* from FlyBase ID: FBti0099948; *traffic jam-Gal4* from DGRC: 104055; *FRTG13* from BDSC: 1956; *Ubi-mRFP.nls* from BDSC: 35496
D. melanogaster. y[1] w[*]; P{w[+mC]=UASp-YFP.Rab10}21	Bloomington Drosophila Stock Center (Zhang et al., 2007)	BDSC: 9789; FlyBase ID: FBal0215407
D. melanogaster. w[*]; P{w[+mC]=UAS-ChRFP-Tub}2	Bloomington Drosophila Stock Center	BDSC: 25774; FlyBase ID: FBst0025774
D. melanogaster. w[1118] TI{TI}Rab10[EYFP]	Bloomington Drosophila Stock Center (Dunst et al., 2015)	BDSC: 62548; FlyBaseID: FBst0062548
D. melanogaster. Ubi-Jupiter-mCherry (III)	Laboratory of Vladimir I. Gelfand (Lu et al., 2013.)	FlyBase ID: FBtp0085844
D. melanogaster. UAS-RFP-Rab10 (II)	Isabella et al., 2016.	
D. melanogaster. PBac{Khc-73^{fTRG01377}.sfGFP-TVPTBF} VK00033	Vienna Drosophila Resource Collection (Sarov et al., 2016)	VDRC: 318350; FlyBase ID: FBal0339158
D. melanogaster. P{UASt-Khc-73.HA} (III)	Laboratory of Chris Q. Doe (Siegrist and Doe, 2005.)	FlyBase ID: FBal0193854

D. melanogaster. w1118; PBac{602.P.SVS-1}Pdi^{CPTI000688}	Vienna Drosophila Resource Collection	VDRC: 115041; FlyBase ID: FBal0262348
D. melanogaster. w[*]; P{w[+mC]=Ubi-p63E-Patronin.A.GFP}3M/TM3, Sb[1]	Bloomington Drosophila Stock Center (Wang et al., 2013.)	BDSC: 55129; FlyBase ID: FBal0290910
D. melanogaster. w[1118]; P{w[+mC]=PTT-GA}Jupiter[G00147].	Bloomington Drosophila Stock Center, Flytrap (Morin et al., 2001)	BDSC:6836; FlyBase ID: FBal0148245
D. melanogaster. *Klc*^{RNAi} : y[1] sc[*] v[1] sev[21]; P{y[+t7.7] v[+t1.8]=TRiP.HMS00883}attP2	Bloomington Drosophila Stock Center	BDSC: 33934; FlyBase ID: FBal0257559
D. melanogaster. *Khc*^{RNAi} : y[1] sc[*] v[1] sev[21]; P{y[+t7.7] v[+t1.8]=TRiP.GL00330}attP2	Bloomington Drosophila Stock Center	BDSC: 35409; FlyBase ID: FBal0262797
D. melanogaster. w[*];P{w[+mW.hs]=FRT(w[hs])}G13 Khc^{27}/Cyo	Brendza et al., 1999.	FlyBase ID: FBal0101625
D. melanogaster. w[*];P{w[+mW.hs]=FRT(w[hs])}G13 TI{TI}KhcKO.mutA/Cyo	Laboratory of Vladimir I. Gelfand (Winding et al., 2016.)	BDSC: 79036; FlyBase ID: FBal0326706
D. melanogaster. w[*]; P{w[+mC]=UASp-RFP.KDEL}10/TM3, Sb[1]	Bloomington Drosophila Stock Center	BDSC: 30909; FlyBase ID: FBst0030909
Recombinant DNA		
Plasmid: pU6-BbsI-chiRNA	Laboratories of Melissa Harrison & Kate O'Connor-Giles & Jill Wildonger (Gratz et al., 2013.)	Addgene plasmid # 45946 ; RRID:Addgene_45946
Plasmid: pU6 guide Khc-73 exon 3, see Methods S1, Table S3	This study	
Plasmid: pU6 guide Khc-73 exon 4, see Methods S1, Table S3	This study	
Primers and smiFISH probe sequences are listed in Supplemental Table 3.		
Software and Algorithms		
Fiji	Schindelin et al., 2012.	https:/fiji.sc
HandBrake 1.3.3 The open source video transcoder	HandBrake Team	https://handbrake.fr/
Zen Blue	Zeiss	
Zen Black	Zeiss	
MetaMorph	Molecular Devices	
MATLAB R2020a	MathWorks	
MATLAB Sobel operator function	Li and Munro, 2020.	

Prism8 and Prism9 for MacOS	GraphPad Software, LLC	
Microsoft Excel for Mac, version 16.45	Microsoft	

1002

1003 **SUPPLEMENTAL ITEMS LEGENDS**
1004
1005 **Supplemental Table 3. Sequences of reagents used for CRISPR of Khc-73, *Khc-73$^{3-3}$* allele, and**
1006 **smiFISH probes, related to Figure S1B and Method Details.**
1007 Supplemental excel sheet
1008
1009 **Movie 1. Background information on follicle cell migration and BM fibril deposition**
1010 Section 1 shows a confocal time-lapse taken along the basal surface of follicle cells in a stage 7 egg
1011 chamber. The BM is visualized with Col IV-GFP and cell edges are stained with CellMask. Follicle cells
1012 collectively migrate along the static BM (Haigo and Bilder, 2011). Section 2 diagrams how newly
1013 secreted BM proteins form fibrils in the space between cells, which then attach and are pulled on the
1014 BM as cells migrate (Isabella and Horne-Badovinac, 2016). Section 3 shows a time-lapse of fibril
1015 deposition. The BM is visualized with Col IV-GFP and cell edges are stained with CellMask. The BM
1016 has been bleached to facilitate visualization of newly deposited fibrils. Fibrils are manually highlighted
1017 with colored lines. As shown in Isabella and Horne-Badovinac, 2016).
1018
1019 **Movie 2. 3D organization of MTS**
1020 Images from an airyscan confocal z-stack of MTs (anti-acetylated α-tubulin staining) in wild-type follicle
1021 cells. Inferno lookup table (LUT) represents intensity of MT staining. Movie starts at the basal surface
1022 and steps through the full- thickness of the epithelium. This is followed by repeating this stack with a
1023 focus on a single cell. The yellow box highlights the leading edge of the cell where MT bundles bend
1024 and integrate with the apical-basal MT array. A 3D projection of this yellow-boxed region follows the
1025 image stack. Stage 7 wild-type egg chamber. Scale bar, 10 μm.
1026
1027 **Movie 3. YFP-Rab10+ compartments move along MTs at the basal surface of follicle cells**
1028 Spinning disk confocal time-lapse of UAS-YFP-Rab10 and UAS-ChRFP-Tubulin dynamics along the
1029 basal surface of follicle cells. YFP-Rab10+ structures move rapidly along MTs and concentrate at the
1030 basal trailing edge of cells. Near the leading edge of cells, MTs appear to fade from view. Motile YFP-
1031 Rab10+ punctae appear and disappear in these regions. Stage 8 egg chamber. The tissue is also
1032 collectively migrating towards the bottom of the screen. Scale bar, 10 μm.
1033
1034 **Movie 4. Dynamic YFP-Rab10+ structures move into and out of HA-Khc-73-induced foci**
1035 Partial TIRF time-lapse of UAS-YFP-Rab10 in cells also overexpressing UAS-HA-Khc-73 taken along
1036 the basal surface of follicle cells. Relative intensity of the YFP-Rab10 signal is displayed using the
1037 inferno lookup table (LUT). A continuous 200 ms stream of images was collected to follow the rapid
1038 tubulovesicular dynamics in and out of the ectopic foci of YFP-Rab10 induced by overexpression of HA-
1039 Khc-73. The tissue is collectively migrating towards the bottom of the screen, but moves little over this
1040 time scale. Stage 7 egg chamber. Scale bar, 5 μm.
1041
1042 **Movie 5. Dynamics of YFP-Rab10+ compartments at the basal surface of control and *Khc-73$^{3-3}$***
1043 **follicle cells**
1044 *Section 1*
1045 Partial TIRF time-lapse of UAS-YFP-Rab10 with the cell edges labeled with CellMask. Images are
1046 taken every 15 sec to visualize how YFP-Rab10+ compartments are dynamically maintained at basal

1047 trailing edges as cells migrate. YFP-Rab10+ compartments are reduced at the basal surface of *Khc-*
1048 *73*$^{3-3}$ cells in comparison to controls. However, *Khc-73*$^{3-3}$ cells still have a smaller population YFP-
1049 Rab10+ compartments that appear at the basal surface and collect near the basal trailing cell edges.
1050 Stage 7 egg chambers. Scale bar, 10 μm.
1051 *Section 2*
1052 Partial TIRF time-lapse of UAS-YFP-Rab10 in the same egg chambers imaged every 1 second to allow
1053 tracking of individual YFP-Rab10+ puncta movements. YFP-Rab10+ punctae move rapidly towards
1054 both the trailing and leading edges of cells. Although there is less overall YFP-Rab10+ compartment
1055 accumulation at the basal surface of *Khc-73*$^{3-3}$ cells, the punctae present do move rapidly. Stage 7 egg
1056 chambers. Scale bar, 10 μm.
1057 *Section 3*
1058 Partial TIRF time-lapse of UAS-YFP-Rab10 along the basal surface. Images are taken every 1 sec.
1059 Two example cells were selected to show Rab10+ puncta trajectories. Trajectories are overlaid in the
1060 left panel and the original image is shown on the right. Cells are outlined in yellow at beginning of movie
1061 for orientation. The control time-lapse is followed by the *Khc-73*$^{3-3}$ time-lapse. Stage 7 egg chambers.
1062 Scale bars, 5 μm.
1063
1064 **Movie 6. BM cables act as anchors that impede cell migration, deforming cells and nuclei**
1065 A confocal z-stack beginning at the basal surface shows that the Col IV-GFP in a control egg chamber
1066 is mainly found in the plane at the basal surface. Follicle cells are hexagonally packed (anti-Dlg) and
1067 nuclei (DAPI) are round. In the *Khc-73*$^{3-3}$ egg chamber, a region with several cables of Col IV-GFP
1068 running from the basal BM to the apical surface deforms cell edges and nuclei. Stage 8 egg chamber.
1069 Scale bar, 5 μm.

1070 **REFERENCES**
1071

1072 Ahmed, S.M., and Macara, I.G. (2017). The Par3 polarity protein is an exocyst receptor essential for mammary
1073 cell survival. Nat Commun *8*, 14867.

1074 Almeida, J.B.D., and Stow, J.L. (1991). Disruption of microtubules alters polarity of basement membrane
1075 proteoglycan secretion in epithelial cells. Am J Physiol-Cell Ph *261*, C691–C700.

1076 Arpağ, G., Shastry, S., Hancock, W.O., and Tüzel, E. (2014). Transport by Populations of Fast and Slow Kinesins
1077 Uncovers Novel Family-Dependent Motor Characteristics Important for In Vivo Function. Biophys J *107*, 1896–
1078 1904.

1079 Arpağ, G., Norris, S.R., Mousavi, S.I., Soppina, V., Verhey, K.J., Hancock, W.O., and Tüzel, E. (2019). Motor
1080 Dynamics Underlying Cargo Transport by Pairs of Kinesin-1 and Kinesin-3 Motors. Biophys J *116*, 1115–1126.

1081 Aurich, F., and Dahmann, C. (2016). A Mutation in fat2 Uncouples Tissue Elongation from Global Tissue Rotation.
1082 Cell Reports *14*, 2503–2510.

1083 Boll, W., Partin, J.S., Katz, A.I., Caplan, M.J., and Jamieson, J.D. (1991). Distinct pathways for basolateral
1084 targeting of membrane and secretory proteins in polarized epithelial cells. Proc National Acad Sci *88*, 8592–8596.

1085 Brendza, K.M., Rose, D.J., Gilbert, S.P., and Saxton, W.M. (1999). Lethal Kinesin Mutations Reveal Amino Acids
1086 Important for ATPase Activation and Structural Coupling. J Biol Chem *274*, 31506–31514.

1087 Budaitis, B.G., Jariwala, S., Rao, L., Yue, Y., Sept, D., Verhey, K.J., and Gennerich, A. (2021). Pathogenic
1088 mutations in the kinesin-3 motor KIF1A diminish force generation and movement through allosteric mechanisms.
1089 J Cell Biol *220*.

1090 Burute, M., and Kapitein, L.C. (2019). Cellular Logistics: Unraveling the Interplay Between Microtubule
1091 Organization and Intracellular Transport. Annu Rev Cell Dev Bi *35*, 1–26.

1092 Buszczak, M., Paterno, S., Lighthouse, D., Bachman, J., Planck, J., Owen, S., Skora, A.D., Nystul, T.G., Ohlstein,
1093 B., Allen, A., et al. (2007). The Carnegie Protein Trap Library: A Versatile Tool for Drosophila Developmental
1094 Studies. Genetics *175*, 1505–1531.

1095 Campos, F.C., Dennis, C., Alégot, H., Fritsch, C., Isabella, A., Pouchin, P., Bardot, O., Horne-Badovinac, S., and
1096 Mirouse, V. (2020). Oriented basement membrane fibrils provide a memory for F-actin planar polarization via the
1097 Dystrophin-Dystroglycan complex during tissue elongation. Dev Camb Engl *147*, dev186957.

1098 Cetera, M., Lewellyn, L., and Horne-Badovinac, S. (2016). Methods in Molecular Biology. Methods Mol Biology
1099 Clifton N J *1478*, 215–226.

1100 Chen, D.-Y., Lipari, K.R., Dehghan, Y., Streichan, S.J., and Bilder, D. (2016). Symmetry Breaking in an Edgeless
1101 Epithelium by Fat2-Regulated Microtubule Polarity. Cell Reports *15*, 1125–1133.

1102 Chen, Y., Wang, Y., Zhang, J., Deng, Y., Jiang, L., Song, E., Wu, X.S., Hammer, J.A., Xu, T., and Lippincott-
1103 Schwartz, J. (2012). Rab10 and myosin-Va mediate insulin-stimulated GLUT4 storage vesicle translocation in
1104 adipocytes. J Cell Biology *198*, 545–560.

1105 Chlasta, J., Milani, P., Runel, G., Duteyrat, J.-L., Arias, L., Lamiré, L.-A., Boudaoud, A., and Grammont, M.
1106 (2017). Variations in basement membrane mechanics are linked to epithelial morphogenesis. Development *144*,
1107 dev.152652.

1108 Clark, I.E., and Jan, L.Y.J. and Y.N. (1997). Reciprocal localization of Nod and kinesin fusion proteins indicates
1109 microtubule polarity in the Drosophila oocyte, epithelium, neuron and muscle. Development 461–470.

1110 Crest, J., Diz-Muñoz, A., Chen, D.-Y., Fletcher, D.A., and Bilder, D. (2017). Organ sculpting by patterned
1111 extracellular matrix stiffness. Elife *6*, e24958.

1112 Danysh, B.P., and Duncan, M.K. (2009). The lens capsule. Exp Eye Res *88*, 151–164.

1113 Denef, N., Chen, Y., Weeks, S.D., Barcelo, G., and Schüpbach, T. (2008). Crag Regulates Epithelial Architecture
1114 and Polarized Deposition of Basement Membrane Proteins in Drosophila. Dev Cell *14*, 354–364.

1115 Deng, C.-Y., Lei, W.-L., Xu, X.-H., Ju, X.-C., Liu, Y., and Luo, Z.-G. (2014). JIP1 Mediates Anterograde Transport
1116 of Rab10 Cargos during Neuronal Polarization. J Neurosci *34*, 1710–1723.

1117 Devergne, O., Tsung, K., Barcelo, G., and Schüpbach, T. (2014). Polarized deposition of basement membrane
1118 proteins depends on Phosphatidylinositol synthase and the levels of Phosphatidylinositol 4,5-bisphosphate. Proc
1119 National Acad Sci *111*, 7689–7694.

1120 Devergne, O., Sun, G.H., and Schüpbach, T. (2017). Stratum, a Homolog of the Human GEF Mss4, Partnered
1121 with Rab8, Controls the Basal Restriction of Basement Membrane Proteins in Epithelial Cells. Cell Reports *18*,
1122 1831–1839.

1123 Doerflinger, H., Benton, R., Shulman, J.M., and Johnston, D.S. (2003). The role of PAR-1 in regulating the
1124 polarised microtubule cytoskeleton in the Drosophila follicular epithelium. Development *130*, 3965–3975.

1125 Dunst, S., Kazimiers, T., von Zadow, F., Jambor, H., Sagner, A., Brankatschk, B., Mahmoud, A., Spannl, S.,
1126 Tomancak, P., Eaton, S., et al. (2015). Endogenously Tagged Rab Proteins: A Resource to Study Membrane
1127 Trafficking in Drosophila. Dev Cell *33*, 351–365.

1128 Etoh, K., and Fukuda, M. (2019). Rab10 regulates tubular endosome formation through KIF13A/B motors. J Cell
1129 Sci *132*, jcs.226977.

1130 Fourriere, L., Kasri, A., Gareil, N., Bardin, S., Bousquet, H., Pereira, D., Perez, F., Goud, B., Boncompain, G., and
1131 Miserey-Lenkei, S. (2019). RAB6 and microtubules restrict protein secretion to focal adhesions. J Cell Biology
1132 *218*, 2215–2231.

1133 Fu, M., and Holzbaur, E.L.F. (2014). Integrated regulation of motor-driven organelle transport by scaffolding
1134 proteins. Trends Cell Biol *24*, 564–574.

1135 Gonzalez, and Woods (2017). Digital Image Processing, 4 ed. Pearson (Pearson).

1136 Gratz, S.J., Cummings, A.M., Nguyen, J.N., Hamm, D.C., Donohue, L.K., Harrison, M.M., Wildonger, J., and
1137 O'Connor-Giles, K.M. (2013). Genome Engineering of Drosophila with the CRISPR RNA-Guided Cas9 Nuclease.
1138 Genetics *194*, 1029–1035.

1139 Gratz, S.J., Ukken, F.P., Rubinstein, C.D., Thiede, G., Donohue, L.K., Cummings, A.M., and O'Connor-Giles,
1140 K.M. (2014). Highly Specific and Efficient CRISPR/Cas9-Catalyzed Homology-Directed Repair in Drosophila.
1141 Genetics *196*, 961–971.

1142 Guardia, C.M., Farías, G.G., Jia, R., Pu, J., and Bonifacino, J.S. (2016). BORC Functions Upstream of Kinesins 1
1143 and 3 to Coordinate Regional Movement of Lysosomes along Different Microtubule Tracks. Cell Reports *17*,
1144 1950–1961.

1145 Guedes-Dias, P., Nirschl, J.J., Abreu, N., Tokito, M.K., Janke, C., Magiera, M.M., and Holzbaur, E.L.F. (2019).
1146 Kinesin-3 Responds to Local Microtubule Dynamics to Target Synaptic Cargo Delivery to the Presynapse. Curr
1147 Biol *29*, 268-282.e8.

1148 Gutzeit, H.O. (1991). Organization and in vitro activity of microfilament bundles associated with the basement
1149 membrane of Drosophila follicles. Acta Histochem Suppl *41*, 201–210.

1150 Haigo, S.L., and Bilder, D. (2011). Global Tissue Revolutions in a Morphogenetic Movement Controlling
1151 Elongation. Science *331*, 1071–1074.

1152 Hancock, W.O. (2014). Bidirectional cargo transport: moving beyond tug of war. Nat Rev Mol Cell Bio *15*, 615–
1153 628.

1154 Horne-Badovinac, S., and Bilder, D. (2005). Mass transit: epithelial morphogenesis in the Drosophila egg
1155 chamber. Dev Dyn Official Publ Am Assoc Anatomists *232*, 559–574.

1156 Huckaba, T.M., Gennerich, A., Wilhelm, J.E., Chishti, A.H., and Vale, R.D. (2011). Kinesin-73 Is a Processive
1157 Motor That Localizes to Rab5-containing Organelles*. J Biological Chem *286*, 7457–7467.

1158 Isabella, A.J., and Horne-Badovinac, S. (2016). Rab10-Mediated Secretion Synergizes with Tissue Movement to
1159 Build a Polarized Basement Membrane Architecture for Organ Morphogenesis. Dev Cell *38*, 47–60.

1160 Jayadev, R., and Sherwood, D.R. (2017). Basement membranes. Curr Biol *27*, R207–R211.

1161 Jolly, A.L., Kim, H., Srinivasan, D., Lakonishok, M., Larson, A.G., and Gelfand, V.I. (2010). Kinesin-1 heavy chain
1162 mediates microtubule sliding to drive changes in cell shape. Proc National Acad Sci *107*, 12151–12156.

1163 Kamal, A., and Goldstein, L.S.B. (2002). Principles of cargo attachment to cytoplasmic motor proteins. Curr Opin
1164 Cell Biol *14*, 63–68.

1165 Khanal, I., Elbediwy, A., Loza, M. del C.D. de la, Fletcher, G.C., and Thompson, B.J. (2016). Shot and Patronin
1166 polarise microtubules to direct membrane traffic and biogenesis of microvilli in epithelia. J Cell Sci *129*, 2651–
1167 2659.

1168 Kohrs, F.E., Daumann, I.-M., Pavlović, B., Jin, E.J., Lin, S.-C., Port, F., Kiral, F.R., Wolfenberg, H., Mathejczyk,
1169 T.F., Chan, C.-C., et al. (2020). Systematic functional analysis of Rab GTPases reveals limits of neuronal
1170 robustness in Drosophila. Biorxiv 2020.02.21.959452.

1171 Kozyrina, A.N., Piskova, T., and Russo, J.D. (2020). Mechanobiology of Epithelia From the Perspective of
1172 Extracellular Matrix Heterogeneity. Frontiers Bioeng Biotechnology *8*, 596599.

1173 Kreitzer, G., and Myat, M.M. (2018). Microtubule Motors in Establishment of Epithelial Cell Polarity. Csh Perspect
1174 Biol *10*, a027896.

1175 Kreitzer, G., Schmoranzer, J., Low, S.H., Li, X., Gan, Y., Weimbs, T., Simon, S.M., and Rodriguez-Boulan, E.
1176 (2003). Three-dimensional analysis of post-Golgi carrier exocytosis in epithelial cells. Nat Cell Biol *5*, 126–136.

1177 Lee, M.-C., and Spradling, A.C. (2014). The progenitor state is maintained by lysine-specific demethylase 1-
1178 mediated epigenetic plasticity during Drosophila follicle cell development. Gene Dev *28*, 2739–2749.

1179 Lee, M.-C., Skora, A.D., and Spradling, A.C. (2017). Identification of Genes Mediating Drosophila Follicle Cell
1180 Progenitor Differentiation by Screening for Modifiers of GAL4::UAS Variegation. G3 Genes Genomes Genetics *7*,
1181 309–318.

1182 Lerner, D.W., McCoy, D., Isabella, A.J., Mahowald, A.P., Gerlach, G.F., Chaudhry, T.A., and Horne-Badovinac, S.
1183 (2013). A Rab10-Dependent Mechanism for Polarized Basement Membrane Secretion during Organ
1184 Morphogenesis. Dev Cell *24*, 159–168.

1185 Li, Y., and Munro, E. (2020). Existing actin filaments orient new filament growth to provide structural memory of
1186 filament alignment during cytokinesis. Biorxiv 2020.04.13.039586.

1187 Liao, E.H., Gray, L., Tsurudome, K., Mounzer, W.E., Elazzouzi, F., Baim, C., Farzin, S., Calderon, M.R., Kauwe,
1188 G., and Haghighi, A.P. (2018). Kinesin Khc-73/KIF13B modulates retrograde BMP signaling by influencing
1189 endosomal dynamics at the Drosophila neuromuscular junction. Plos Genet *14*, e1007184.

1190 Lord, S.J., Velle, K.B., Mullins, R.D., and Fritz-Laylin, L.K. (2020). SuperPlots: Communicating reproducibility and
1191 variability in cell biology. J Cell Biol *219*.

1192 Lu, W., Fox, P., Lakonishok, M., Davidson, M.W., and Gelfand, V.I. (2013). Initial Neurite Outgrowth in Drosophila
1193 Neurons Is Driven by Kinesin-Powered Microtubule Sliding. Curr Biol *23*, 1018–1023.

1194 Miner, J.H. (2012). The glomerular basement membrane. Exp Cell Res *318*, 973–978.

1195 Monroy, B.Y., Tan, T.C., Oclaman, J.M., Han, J.S., Simó, S., Niwa, S., Nowakowski, D.W., McKenney, R.J., and
1196 Ori-McKenney, K.M. (2020). A Combinatorial MAP Code Dictates Polarized Microtubule Transport. Dev Cell *53*,
1197 60-72.e4.

1198 Morin, X., Daneman, R., Zavortink, M., and Chia, W. (2001). A protein trap strategy to detect GFP-tagged proteins
1199 expressed from their endogenous loci in Drosophila. Proc National Acad Sci *98*, 15050–15055.

1200 Nashchekin, D., Fernandes, A.R., and St Johnston, D. (2016). Patronin/Shot Cortical Foci Assemble the
1201 Noncentrosomal Microtubule Array that Specifies the Drosophila Anterior-Posterior Axis. Dev Cell *38*, 61–72.

1202 Norris, S.R., Soppina, V., Dizaji, A.S., Schimert, K.I., Sept, D., Cai, D., Sivaramakrishnan, S., and Verhey, K.J.
1203 (2014). A method for multiprotein assembly in cells reveals independent action of kinesins in complex. J Cell
1204 Biology *207*, 393–406.

1205 Polishchuk, R., Pentima, A.D., and Lippincott-Schwartz, J. (2004). Delivery of raft-associated, GPI-anchored
1206 proteins to the apical surface of polarized MDCK cells by a transcytotic pathway. Nat Cell Biol *6*, 297–307.

1207 Ramos-Lewis, W., and Page-McCaw, A. (2018). Basement membrane mechanics shape development: Lesson
1208 from the fly. Matrix Biol *75–76*, 72–81.

1209 Reed, N.A., Cai, D., Blasius, T.L., Jih, G.T., Meyhofer, E., Gaertig, J., and Verhey, K.J. (2006). Microtubule
1210 Acetylation Promotes Kinesin-1 Binding and Transport. Curr Biol *16*, 2166–2172.

1211 Rodriguez-Boulan, E., and Macara, I.G. (2014). Organization and execution of the epithelial polarity programme.
1212 Nat Rev Mol Cell Bio *15*, 225–242.

1213 Sanchez, A.D., and Feldman, J.L. (2017). Microtubule-organizing centers: from the centrosome to non-
1214 centrosomal sites. Curr Opin Cell Biol *44*, 93–101.

1215 Sanes, J.R. (2003). The Basement Membrane/Basal Lamina of Skeletal Muscle. J Biol Chem *278*, 12601–12604.

1216 Sarov, M., Barz, C., Jambor, H., Hein, M.Y., Schmied, C., Suchold, D., Stender, B., Janosch, S., KJ, V.V.,
1217 Krishnan, R., et al. (2016). A genome-wide resource for the analysis of protein localisation in Drosophila. Elife *5*,
1218 e12068.

1219 Schindelin, J., Arganda-Carreras, I., Frise, E., Kaynig, V., Longair, M., Pietzsch, T., Preibisch, S., Rueden, C.,
1220 Saalfeld, S., Schmid, B., et al. (2012). Fiji: an open-source platform for biological-image analysis. Nat Methods *9*,
1221 676–682.

1222 Schuck, S., Gerl, M.J., Ang, A., Manninen, A., Keller, P., Mellman, I., and Simons, K. (2007). Rab10 is Involved in
1223 Basolateral Transport in Polarized Madin–Darby Canine Kidney Cells. Traffic *8*, 47–60.

1224 Serra-Marques, A., Martin, M., Katrukha, E.A., Grigoriev, I., Peeters, C.A., Liu, Q., Hooikaas, P.J., Yao, Y.,
1225 Solianova, V., Smal, I., et al. (2020). Concerted action of kinesins KIF5B and KIF13B promotes efficient secretory
1226 vesicle transport to microtubule plus ends. Elife *9*, e61302.

1227 Sherwood, N.T., Sun, Q., Xue, M., Zhang, B., and Zinn, K. (2004). Drosophila Spastin Regulates Synaptic
1228 Microtubule Networks and Is Required for Normal Motor Function. Plos Biol *2*, e429.

1229 Siddiqui, N., and Straube, A. (2017). Intracellular cargo transport by kinesin-3 motors. Biochem Mosc *82*, 803–
1230 815.

1231 Siegrist, S.E., and Doe, C.Q. (2005). Microtubule-Induced Pins/Gαi Cortical Polarity in Drosophila Neuroblasts.
1232 Cell *123*, 1323–1335.

1233 Skora, A.D., and Spradling, A.C. (2010). Epigenetic stability increases extensively during Drosophila follicle stem
1234 cell differentiation. Proc National Acad Sci *107*, 7389–7394.

1235 Soppina, V., Norris, S.R., Dizaji, A.S., Kortus, M., Veatch, S., Peckham, M., and Verhey, K.J. (2014). Dimerization
1236 of mammalian kinesin-3 motors results in superprocessive motion. Proc National Acad Sci *111*, 5562–5567.

1237 Stenmark, H. (2009). Rab GTPases as coordinators of vesicle traffic. Nat Rev Mol Cell Bio *10*, 513–525.

1238 Tsanov, N., Samacoits, A., Chouaib, R., Traboulsi, A.-M., Gostan, T., Weber, C., Zimmer, C., Zibara, K., Walter,
1239 T., Peter, M., et al. (2016). smiFISH and FISH-quant – a flexible single RNA detection approach with super-
1240 resolution capability. Nucleic Acids Res *44*, e165–e165.

1241 Viktorinová, I., and Dahmann, C. (2013). Microtubule Polarity Predicts Direction of Egg Chamber Rotation in
1242 Drosophila. Curr Biol *23*, 1472–1477.

1243 Walma, D.A.C., and Yamada, K.M. (2020). The extracellular matrix in development. Development *147*,
1244 dev175596.

1245 Wang, H., Brust-Mascher, I., Civelekoglu-Scholey, G., and Scholey, J.M. (2013). Patronin mediates a switch from
1246 kinesin-13–dependent poleward flux to anaphase B spindle elongation. J Cell Biology *203*, 35–46.

1247 Winding, M., Kelliher, M.T., Lu, W., Wildonger, J., and Gelfand, V.I. (2016). Role of kinesin-1–based microtubule
1248 sliding in Drosophila nervous system development. Proc National Acad Sci *113*, E4985–E4994.

1249 Zhang, J., Schulze, K.L., Hiesinger, P.R., Suyama, K., Wang, S., Fish, M., Acar, M., Hoskins, R.A., Bellen, H.J.,
1250 and Scott, M.P. (2007). Thirty-One Flavors of Drosophila Rab Proteins. Genetics *176*, 1307–1322.

1251 Zou, W., Yadav, S., DeVault, L., Jan, Y.N., and Sherwood, D.R. (2015). RAB-10-Dependent Membrane Transport
1252 Is Required for Dendrite Arborization. Plos Genet *11*, e1005484.

1253